Regional modeling of internal tide dynamics around New Caledonia: energetics and sea surface height signature

Arne Bendinger[1], Sophie Cravatte[1], Lionel Gourdeau[1], Laurent Brodeau[2,a], Aurélie Albert[2], Michel Tchilibou[1,b], Florent Lyard[1], and Clément Vic[3]

[1]Université de Toulouse, LEGOS (CNES/CNRS/IRD/UPS), Toulouse, France
[2]Université Grenoble Alpes, CNRS, INRAE, IRD, Grenoble INP, Institut des Géosciences de l'Environnement, Grenoble, France
[3]Laboratoire d'Océanographie Physique et Spatiale, Univ. Brest, CNRS, Ifremer, IRD, Plouzané, France
[a]now at: DATLAS, Grenoble, France
[b]now at: CLS, Ramonville Saint-Agne, France

Correspondence: Arne Bendinger (arne.bendinger@legos.obs-mip.fr)

Abstract. The Southwestern Tropical Pacific exhibits a complex bathymetry and represents a hot spot of internal tide generation. Based on a tailored high-resolution regional model, we investigate for the first time the internal tide field around the New Caledonia islands through energy budgets that quantify the internal tide generation, propagation, and dissipation. A total of 15.97 GW is converted from the barotropic to the baroclinic tide with the main conversion sites associated with the

5   most prominent bathymetric structures such as continental slopes and narrow passages in the north (2.17 GW) and ridges and seamounts south of New Caledonia (3.92 GW). The bulk of baroclinic energy is generated in shallow waters around 500 m depth and on critical to supercritical slopes highlighting the limitations of linear semi-analytical models in those areas. Despite the strongly dominant mode-1 generation, more than 50 % of the locally generated energy dissipates in the near-field close to the generation sites. The remaining energy propagates within well-defined tidal beams with baroclinic energy fluxes of up

10   to 30 kW m^{-1} toward the open ocean, strongly dominated by mode-1. The energetic mesoscale eddy activity in the region appears to be the main source of tidal incoherence. Locally, mesoscale eddy-driven stratification changes induce variations of the conversion term. In the far-field, incoherence of the energy flux arises through the interaction of the tidal beam with the eddying background flow. The New Caledonia site represents a challenge for SWOT (Surface Water Ocean Topography) observability of meso- and submesoscale dynamics in the presence of internal tides with sea surface height signatures > 6 cm.

15   We show that a correction of the coherent baroclinic tide may improve the observability range by shifting the transition scale between balanced and unbalanced flow in winter from 180 km to 50-80 km. In contrast, in summer observability increases only marginally due to the seasonally amplified signature of the incoherent tide at scales below 100 km.

1   Introduction

The flow of barotropic tidal oceanic currents over bathymetry such as continental slopes, ridges, and seamounts represent a

20   major source for baroclinic energy in the global ocean in form of internal tides (i.e. internal waves at tidal frequency) expressed by high-frequency fluctuations and vertical displacements of isopycnal surfaces (Bell Jr, 1975; Smith and Young, 2002; Garrett

and Kunze, 2007). From a global point of view, internal tides have received increasing attention in recent decades as they provide a route to energy dissipation away from lateral boundaries and the surface through diapycnal mixing. Hence, they drive deep ocean mixing while closing the global oceanic energy budget and the meridional overturning circulation (Melet et al.,

25 2013; Kunze, 2017a, b). It is suggested that internal tides provide around 1 TW of energy away from the continental shelves accounting for approximately half of the estimated energy (2 TW) which is required to maintain the abyssal stratification (Munk and Wunsch, 1998; Egbert and Ray, 2001; Jayne and St. Laurent, 2001; Nycander, 2005; Waterhouse et al., 2014; Kunze, 2017b).

Internal tides express in vertical oscillations of density surfaces with strong baroclinic sheared velocities. They are characterized

30 by a complex vertical structure that can be described by a discrete set of vertical normal modes via the Sturm-Liouville problem (Kelly, 2016; Arbic et al., 2018). Low-vertical modes have large horizontal wavelengths ($\mathcal{O}$(150 km)), usually form over large-scale topographic features, and propagate over large distances ($\mathcal{O}$(1000 km)); Dushaw et al., 1995; St. Laurent and Garrett, 2002; Alford, 2003; Zhao et al., 2010, 2016). In contrast, high-vertical modes feature smaller horizontal wavelengths that are generated over smaller-scale topographic features. They tend to dissipate locally not far away from the formation sites due

35 to their lower group velocities and higher vertical shear (Zhao et al., 2016; Vic et al., 2019). Characterizing internal tides, their vertical structure and propagation is thus key to better understand their contribution to mixing. Yet, it is still challenging, both through observations or model experiments. Some scattered in-situ observations with high-frequency sampling, such as moorings, can help to characterize these processes at some locations (e.g., Zilberman et al., 2011; Vic et al., 2018) but they do not provide a global view. Alternatively, altimetry Sea Surface Height (SSH) observations have been extensively used to

40 estimate globally the SSH imprint of internal tides by using e.g. empirical models that are based on an up to 20-year long record of conventional altimeter missions (Zhao et al., 2016; Ray and Zaron, 2016; Zaron, 2019; Ubelmann et al., 2022). These estimates have provided us with a robust representation of the coherent internal tide which is defined here as the phase-locked internal tide being constant in amplitude and phase, and determined over a long time series. They mostly provide very limited information about the internal tides' vertical structure, allowing the detection of the first and second vertical modes only.

45 The time-varying component and the accompanied departure from tidal coherence is referred to as the incoherent tide or the non-phase locked tide. Locally, incoherence arises through temporal changes in stratification or impinging tides from remote areas that may affect the generation of the internal tides (Zilberman et al., 2011; Kerry et al., 2014, 2016). In addition, incoherence occurs when the propagating internal tide interacts with the background (varying) circulation, i.e. mid-latitude and equatorial jets, as well as mesoscale features such as eddies (Park and Watts, 2006; Dunphy and Lamb, 2014; Dunphy et al.,

50 2017; Ponte and Klein, 2015; Kelly and Lermusiaux, 2016; Magalhães et al., 2016; Buijsman et al., 2017; Tchilibou et al., 2022; Guo et al., 2023). Using idealized numerical experiments, Ponte and Klein (2015) studied the passage of low-mode internal tides through a turbulent mesoscale eddy field. The authors state that tidal incoherence emerges in the form of complex interference patterns that strengthen with increasing background turbulence. In addition, the interaction between the eddy field and the low-mode internal tide has been suggested to be favored when they feature comparable length scales resulting in energy

55 scattering towards higher modes (Dunphy and Lamb, 2014). It was shown that the incoherent internal tide may represent a large fraction of the total signal in the tropical ocean (Buijsman et al., 2017; Zaron, 2017) and therefore, it largely contributes to

energy propagation and dissipation in the open ocean: its characterization remains an important challenge.

There is an additional reason why better characterization of the internal tide field with its vertical modes (each associated with a different wavelength), and its signature in SSH is an urgent and important task: in preparation of the Surface Water Ocean

60 Topography (SWOT) satellite mission (launched in December 2022) which is expected to provide new insights into small-scale ocean dynamics. SWOT has been designed to resolve wavelengths by up to ten times higher resolution (down to 15 km; Fu et al., 2012; Fu and Ubelmann, 2014) than conventional altimetry ($\mathcal{O}$ 100 km; Ballarotta et al., 2019) with global high-resolution observations of SSH imprints from meso- and submesoscale dynamics, down to high-frequency motions, and the interaction between each other (Fu and Ferrari, 2008; Morrow et al., 2019). The challenge lies in disentangling the measured SSH signal

65 associated with balanced and unbalanced motion, i.e. eddies and gravity waves, since they can feature similar spatial scales. From an oceanographic perspective, the characterization of the meso- and submesoscale circulation is the primary objective of SWOT which will shed light on the small-scale distribution of horizontal kinetic energy as well as vertical transport of heat, momentum, and tracers from the ocean surface to the interior and vice versa (Morrow et al., 2019). The so-called "transition scale" (defined as the separation length scale between dominant balanced or unbalanced motion) was found to strongly vary

70 both geographically and seasonally (Qiu et al., 2018). This is an important quantity as it tells us at what scales the geostrophic assumption is valid or not. In order to properly derive the meso- and submesoscale dynamics, an accurate correction of SSH for high-frequency motions, i.e. internal tides, is suggested (Zaron, 2019; Carrere et al., 2021).

Huge effort has been made in recent years in the SWOT science community to address the SSH signature and observability of internal tides using state-of-the art high-resolution numerical models including tidal forcings, idealized simulations, and linear

75 theory (e.g., Savage et al., 2017; Lahaye et al., 2019; Tchilibou et al., 2022; Wang et al., 2022). Even though the formation sites of internal tides are globally well known, their propagation, dissipation, and interaction with the background circulation need more investigation. The energy converted from barotropic to baroclinic tides, the distribution of the vertical modes generated, the loss of coherence, the local ratio between dissipation and conversion, are all greatly depending on the local bathymetric features and background circulation, and thus on the region studied. Dedicated studies of internal tide characteristics and

80 energetics near internal tide generation hot spots have been conducted in various regions such as the Hawaiian Ridge (Carter et al., 2008), Luzon Strait (Kerry et al., 2013), Solomon Sea (Tchilibou et al., 2020), Amazonian Shelf (Tchilibou et al., 2022) and the Mid-Atlantic Ridge (Lahaye et al., 2020) emphasizing the need for regional focus with high-resolution regional simulations.

Here, we present for the first time in full extent the internal tide field energetics around New Caledonia (in the Southwestern

85 Tropical Pacific) using the output of a high-resolution regional simulation from a full-model calendar year (Fig. 1a). This region deserves a focus for two main reasons: First, the complex bathymetry of large-scale ridges, very steep slopes, shelf breaks, basins, and seamounts at mid-depths and near-surface with varying slopes gives rise to a pronounced and complex internal tide field with propagating beams over several hundreds of km and SSH signatures of > 5 cm (Ray and Zaron, 2016). New Caledonia is also subject to a complex regional circulation (Qu and Lindstrom, 2002; Kessler and Cravatte, 2013; Cravatte

90 et al., 2015). The numerous islands in the Coral Sea serve as obstacles forming boundary currents and westward jets as well as recirculation and eastward counter currents (Couvelard et al., 2008; Qiu et al., 2009). It underlies a strong level of eddy kinetic

energy (EKE) due to barotropic and baroclinic instabilities which in turn arise from sheared current systems (Qiu and Chen, 2004; Qiu et al., 2009) giving rise to non-linear eddy motion (Keppler et al., 2018). Through the interaction with the local eddy dynamics, the internal tide field is potentially subject to a loss of coherence making New Caledonia an interesting site to

95 study eddy-internal tide interactions. This makes New Caledonia a challenging task for SWOT observability. In the framework of SWOT and the Adopt-A-Crossover (AdAC) consortium, New Caledonia will be serving as a calibration and validation (CalVal) site within the fast sampling phase and its associated 1-day repeat orbit (see Fig. 1a) during which an extensive field campaign will be carried out to collect high-resolution in-situ measurements. This represents a unique opportunity to survey the dynamics while addressing SSH observability of eddy-internal tide interactions.

100 Second, New Caledonia is recognized internationally for its outstanding biodiversity. It is surrounded by a 1100 km-long barrier reef enclosing a shallow lagoon (Payri et al., 2019). Internal tides may have important implications for coastal temperatures and marine ecosystems, thriving biological productivity, biodiversity, and overall ecological processes. In detail, it has been suggested that internal tides enhance vertical mixing that intensifies upwelling of nutrient-rich waters to the surface (Wolanski and Pickard, 1985; Leichter et al., 2003) while inducing temperature and oxygen variations which in turn impact the chlorophyll

105 content (Wolanski et al., 2004; Wang et al., 2007; Jan and Chen, 2009; Muacho et al., 2013). Internal tides are supposed to play a major role south of New Caledonia where seamounts and ridges are hotspots of biodiversity providing marine habitats for marine mammals, fish, and small-scale organisms despite the relatively unproductive waters of the tropical ocean (Payri and de Forges, 2006; Ganachaud et al., 2010; Gardes et al., 2014; Menkès et al., 2015; Messié et al., 2022). Observing and understanding the local impact of internal tides on the ecosystem up to high trophic levels is of large socio-economic interest

110 for the island's conservation management of marine protected areas. As a first step to investigate the role of internal tides on the local ecosystem and biogeochemistry, it is required to study in detail the governing dynamics at play, i.e. internal tide formation, propagation, and dissipation, and this study will also contribute to that.

This study is organized as follows. In Sect. 2, we introduce the high-resolution modeling strategy, the tidal analyses and diagnostics used in this study, and the different datasets or products used. The model validation is presented in Sect. 3, where

115 we estimate the model ability to realistically simulate the mean circulation, the mesoscale activity, and the barotropic and baroclinic tides. In Sect. 4, we focus on the M2 semi-diurnal internal tide (largely dominant) energetics, in the region around New Caledonia and in the hot spots of internal tide generation. We quantify tidal incoherence in Sect. 5, and suggest that it arises in both the near-field at the generation site and the far field due to the presence of mesoscale eddy activity. Internal tide SSH signatures are investigated in Sect. 6, in the context of SWOT observability. We finish with a summary and discussion in

120 Sect. 7.

2 Data and Methods

2.1 Model set-up

The model used in this study is based on the Nucleus for European Modeling of the Ocean (NEMO, code version 4.0.6, Madec and Team) which solves the 3-dimensional primitive equations on a staggered Arakawa-C type grid. The model grid consists

125 of a host grid (TROPICO12) at 1/12° horizontal resolution that spans the Pacific Ocean basin from 142° E - 290° E and 24° N
- 46° S (Fig 1a). It features 125 vertical levels with 0.5 m thickness at the surface increasing toward 150 m in the deep ocean
with 75 vertical levels in the upper 1000 m. In the vertical, the model uses a partial step z-coordinate with a non-linear free
surface.

Further, the model set-up features a horizontal grid refinement (nesting), named CALEDO60, at 1/60° horizontal resolution
130 (∼1.7 km grid-box spacing). In this particular region, it is expected to allow the model to be submesoscale-permitting. The
nesting grid is located in the Southwestern Tropical Pacific from 159.2° E - 172.4° E and 15.7° S - 28.8° S and encompasses
New Caledonia (see Fig. 1a). The nesting was set-up using an Adaptive Grid Refinement In Fortran (AGRIF, Debreu et al.,
2008), a tool explicitly designed for NEMO to set up regional simulations embedded in pre-defined configuration. AGRIF
enables the two-way lateral boundary coupling between the host and the nesting grid being integrated sequentially during the
135 whole length of the simulation.

Laplacian isopycnal diffusion coefficients for tracers were chosen to be mesh-size dependent such that the tracer diffusion is
scaled down from the host grid of 93 m^2 s^{-1} to the nesting grid of 4 m^2 s^{-1}. Vertical eddy diffusivity is estimated by a TKE
turbulent closure scheme (Gaspar et al., 1990). It is based on a prognostic equation for turbulent kinetic energy and a closure
assumption for turbulent length scales depending on vertical shear, stratification, vertical diffusion, and dissipation. The ad-
140 vection of momentum is parameterized by means of a third-order scheme based on upstream-biased parabolic interpolation
(UBS).

Initial conditions for temperature and salinity for TROPICO12 and CALEDO60 are prescribed by the GLORYS2V4 oceanic
reanalysis (https://doi.org/10.48670/moi-00023). Atmospheric forcing is taken from ERA5 produced by the European Centre
for Medium-Range Weather Forecasts (ECMWF, Hersbach et al., 2020) provided at hourly temporal resolution and a spatial
145 resolution of 1/4°to compute surface fluxes using bulk formulae and the prognostic sea surface temperature from the model.
Wind stresses are computed following the methodology from Renault et al. (2016), i.e. wind speed minus surface currents,
also know as the current feedback. Both domains are forced by the tidal potential of the five major tidal constituents (M2, S2,
N2, K1, O1). TROPICO12 is forced at its open lateral boundaries with daily currents, temperature, and salinity, likewise using
GLORYS2V4. In addition, TROPICO12 is forced at the open lateral boundaries by SSH and barotropic currents of the same
150 five tidal constituents taken from the global tide atlas FES2014 (Finite Element Solution 2014, Lyard et al., 2021). We made
this limited choice to allow the separation of these constituents at monthly timescales. Recent studies highlighted the impor-
tance of taking into account remote forcing of high-frequency oceanic variability for regional simulations, as it may represent a
non-negligible source of energy (Jeon et al., 2019; Nelson et al., 2019; Mazloff et al., 2020). Further, it was suggested that tidal
accuracy and predictability increase when implementing a two-way nesting framework between the high-resolution regional
155 domain and the lower-resolution host grid (Jeon et al., 2019). The authors show that mass and energy are conserved with no
evident discontinuities along the nesting boundaries.

Apart from increasing predictability through higher horizontal resolution of the nesting grid, it is argued that a realistic
bathymetry product is also essential. For the CALEDO60 domain, we used a specific bathymetric product based on the Smith
and Sandwell (1997) v8.2 dataset (GEBCO20) and a compilation of multibeam echosounder data acquired over the years in

160   the New Caledonia economic zone (Roger et al., 2021). This bathymetric product, initially at 200 m resolution, only covers the area 155° E - 175.1° N, 14.1° S - 26.6° S. It has been combined with the GEBCO20 bathymetry product to cover the full domain.

High-frequency internal waves represent a large source of diapycnal mixing in the open ocean. The associated parameterization scheme developed by St. Laurent et al. (2002) is usually used in NEMO simulations. Here, it has been turned off because our

165   simulation has a resolution large enough to resolve the internal wave dynamics. In fact, it has been recently suggested that turning off background components of the vertical mixing scheme improves the modeled kinetic energy levels (Thakur et al., 2022). The authors show with increasing resolution in the vertical dimension that the internal gravity wave spectra are in better agreement with in-situ observations.

The bottom friction is parameterized using a logarithmic boundary layer with a drag coefficient of 3×10^{-3} (maximum value

170   of 0.1), a roughness of 2.5e-3 m, and a background kinetic energy of 1×10^{-2} m^2 s^{-2}. These values yielded the best visual agreement with respect to the mean regional circulation, i.e. the location and magnitude of zonal jets.

The model has been spun up for two years (model year 2012-2013) before being run for a total of five years (model year 2014-2018). Here, if not noted otherwise, we only focus on 2014 (neutral El Niño - Southern Oscillation conditions) with instantaneous fields saved hourly for the 3-dimensional temperature, salinity, velocity field, and sea surface height for CALEDO60.

175   For TROPICO12, the instantaneous 3-dimensional variables are given at daily resolution, whereas the surface fields are saved at hourly resolution. A twin experiment with identical forcing and parameterization has been initialized, but without barotropic tide forcing. Being subject to a future study, here, it is only used to compare the energy spectrum with the tidal simulation.

2.2   Tidal analysis and diagnostics

2.2.1   Coherent tides

180   In order to investigate the tidal dynamics at play in the regional CALEDO60 simulation, we first apply a harmonic analysis on a full-model calendar year time series (model year 2014) to extract the semidiurnal (M2, S2, N2) and diurnal (K1, O1) tidal constituents. The choice of a full-model calendar year relies upon a compromise between high computational expenses and the representative extraction of the coherent tide through a time series long enough to isolate seasonal and mesoscale variability. Therefore and if not otherwise noted, we define the coherent internal tide as the phase-locked internal tide with

185   constant amplitude and phase referenced to the full-model calendar year time series. Here, we mainly focus our study on the M2 semidiurnal tide which explains in the full-domain more than 80 % of the total energy conversion from the barotropic to the baroclinic tide while representing about 84 % of the semidiurnal energy conversion (Table 1).

The study of internal tides requires an accurate separation of the barotropic and baroclinic tides. The barotropic tide is also known as the surface tide and is directly linked to the astronomical tide forcing. Moreover, it is independent of depth and density

190   stratification (Hendershott, 1981). Introduced in Sect. 1, baroclinic tides (or internal tides) are the result of the barotropic tidal flow over topography in a stratified ocean that express in vertical displacements of isopycnal surfaces at tidal frequencies.

Several approaches to separate barotropic and baroclinic tides have been discussed in detail for example in Kelly et al. (2010),

Nugroho (2017), or in Tchilibou et al. (2020). Here, we use a vertical-mode decomposition approach by solving the Sturm-Liouville problem obeying a linear free-surface while assuming a flat bottom (Kelly and Lermusiaux, 2016):

195
$$\frac{\partial^2 \Phi_n}{\partial z^2} + \frac{N^2}{c_n^2} \Phi_n = 0 \tag{1}$$

$$\Phi_n = \frac{c_n^2}{g} \frac{\partial \Phi_n}{\partial z} \quad \text{at} \quad z = 0, \quad \text{and} \tag{2}$$

$$\Phi_n = 0 \quad \text{at} \quad z = -H, \tag{3}$$

with the given buoyancy frequency N defined as:

$$N^2 = -\frac{g}{\rho_0} \frac{\partial \rho}{\partial z}, \tag{4}$$

200 where ρ is the potential density, z the vertical depth vector, g the gravitational acceleration, and ρ_0 the reference density (1025 kg m^{-3}). c_n is the eigenspeed and Φ_n the eigenfunction describing the vertical structure for vertical velocity and displacement (McDougall and Barker, 2011). It is related to the eigenfuction describing the vertical structure for horizontal velocity and pressure via:

$$\phi_n = \rho_0 \, c_n^2 \, \frac{\partial \Phi_n}{\partial z} \tag{5}$$

205 In practice, the Sturm-Liouville eigenvalue problem has been solved at each grid point of the model, using the annual mean density field referenced to the same period as the harmonic analysis above, for the ten lowest modes, where the lowest mode (n = 0) refers to the barotropic tide and n $\geq$ 1 are the baroclinic modes. Model vertical velocity w, pressure p, horizontal velocity u, v are then decomposed onto the orthogonal, discretized set of normal vertical modes. If not otherwise specified, we define the baroclinic tide as the sum of modes 1-9. As will be seen in Sect. 4, this is sufficient in our study region, where low
210 baroclinic modes are strongly dominant.

2.2.2 Energy equation

The redistribution and transfer of energy from the barotropic tide to the internal tide can be approximated by the barotropic and baroclinic energy equation neglecting the tendency term and nonlinear advection following Simmons et al. (2004), Carter et al. (2008), and Buijsman et al. (2014, 2017) since both terms found to be at least one order of magnitude smaller:

215
$$\nabla_{\mathbf{h}} \cdot \mathbf{F_{bt}} + D_{bt} - C = 0, \tag{6}$$

$$\nabla_{\mathbf{h}} \cdot \mathbf{F_{bc}} + D_{bc} + C = 0, \tag{7}$$

where $\nabla_{\mathbf{h}} \cdot \mathbf{F}$ is the energy flux divergence with $\nabla_{\mathbf{h}} = (\partial/\partial x, \partial/\partial y)$ the horizontal gradient operator and $\mathbf{F} = (F_x, F_y)$ the energy flux vector, D the energy dissipation, and C the barotropic-to-baroclinic conversion term. The subscripts $_{bt}$ and $_{bc}$ stand for the barotropic and baroclinic tide. In the barotropic energy equation, the conversion is considered a sink of energy, whereas
220 it is an energy source in the baroclinic energy equation. The total conversion term is defined as:

$$C = \nabla_{\mathbf{h}} H \langle \mathbf{U} \, p_{bc}(-H) \rangle, \tag{8}$$

where H is the bathymetry, $\mathbf{U} = (U, V)$ the barotropic tidal velocity vector, and p_{bc} the baroclinic tidal pressure at the ocean bottom $(-H)$. $\langle \rangle$ denotes the average over a tidal cycle. Following Zilberman et al. (2009), we compute $< \mathbf{U}\, p_{bc} >$ as follows:

$$< \mathbf{U}\, p_{bc}(-H) > = \frac{1}{2}\, A_{p_{bc}(-H)}\, A_{\mathbf{U}}\, \cos(\phi_{p_{bc}(-H)} - \phi_{\mathbf{U}}), \tag{9}$$

where A and ϕ are the respective amplitude and phase of the tidal harmonic obtained from p_{bc} and $\mathbf{U}$. The conversion for each mode n is given by:

$$C^n = \nabla_{\mathbf{h}} H < \mathbf{U}\, p_{bc}^n(-H) >, \tag{10}$$

where $p_{bc}^n(-H)$ is the baroclinic pressure at the ocean bottom $(-H)$ for mode n. Equivalent to Equation 9, we compute for each mode n:

$$< \mathbf{U}\, p_{bc}^n(-H) > = \frac{1}{2}\, A_{p_{bc}^n(-H)}\, A_{\mathbf{U}}\, \cos(\phi_{p_{bc}^n(-H)} - \phi_{\mathbf{U}}) \tag{11}$$

The propagation of barotropic and baroclinic tide energy is expressed by the energy flux ($\mathbf{F_{bt}}$ and $\mathbf{F_{bc}}$) and is considered here as a depth-integrated quantity:

$$\mathbf{F_{bt}} = \int_{-H}^{\eta} < \mathbf{U}\, p_{bt} > \, dz, \tag{12}$$

$$\mathbf{F_{bc}} = \int_{-H}^{\eta} < \mathbf{u}\, p_{bc} > \, dz, \tag{13}$$

where p_{bt} is the barotropic pressure and $\mathbf{u} = (u, v)$ is the baroclinic velocity vector. Similar to above, we define

$$< \mathbf{U}\, p_{bt} > = \frac{1}{2}\, A_{p_{bt}}\, A_{\mathbf{U}}\, \cos(\phi_{p_{bt}} - \phi_{\mathbf{U}}), \tag{14}$$

$$< \mathbf{u}\, p_{bc} > = \frac{1}{2}\, A_{p_{bc}}\, A_{\mathbf{u}}\, \cos(\phi_{p_{bc}} - \phi_{\mathbf{u}}) \tag{15}$$

The barotropic (D_{bt}) and baroclinic (D_{bc}) dissipation is regarded as the residual of the energy flux divergence and conversion and, hence, obtained through Equation 6 and 7, respectively.

2.2.3 Incoherent tides

In this study, we address internal tide variability, i.e. departure from tidal coherence, which was shown to explain a large fraction of the internal tide variance depending on study region arising from stratification changes and interaction with the background circulation (Kerry et al., 2014, 2016; Buijsman et al., 2017). The easiest approach to infer temporal variability is to perform a harmonic analysis on the full-calendar year from above but subdivided into monthly datasets which is sufficient to disentangle the given semidiurnal and diurnal tidal constituents. The second and more dedicated approach relies on the decomposition of the tidal signal into the coherent and incoherent part, where the incoherent tide is defined as the temporally varying, non-phase

locked tide. Following Buijsman et al. (2017) the coherent barotropic and baroclinic tidal harmonics computed over the 1-year period are first removed from the full model variables (p, u and v). Then, the remaining signals are bandpass filtered at the semidiurnal frequency (10-14 h, Buijsman et al., 2017) to obtain the incoherent semidiurnal internal tide. Addressing the energy flux, the given variables are thus decomposed as follows:

$$\mathbf{u}_{D2} = \mathbf{u}^{coh} + \mathbf{u}^{inc}, \tag{16}$$

$$p_{D2} = p_{bc}^{coh} + p_{bc}^{inc}, \tag{17}$$

where u_{D2} and p_{D2} are representative for the total semidiurnal signal that are composed of the coherent (coh) and the incoherent (inc) contribution. Following Buijsman et al. (2017), the resulting total semidiurnal energy flux can be written as:

$$\mathbf{F}_{D2} = \frac{1}{T} \int\limits_{t_1}^{t_2} \left[\int\limits_{-H}^{\eta} \overbrace{\mathbf{u}^{coh}\, p_{bc}^{coh}}^{\text{coherent}} + \overbrace{\mathbf{u}^{inc}\, p_{bc}^{inc} + \underbrace{\mathbf{u}^{coh}\, p_{bc}^{inc} + \mathbf{u}^{inc}\, p_{bc}^{coh}}_{\text{cross terms}}}^{\text{incoherent}}\, dz \right]\, dt, \tag{18}$$

$$= \mathbf{F}^{coh} + \mathbf{F}^{inc}, \tag{19}$$

where the terms $\mathbf{u}^{coh}\, p_{bc}^{inc} + \mathbf{u}^{inc}\, p_{bc}^{coh}$ represent the cross terms which consider to contribute to the incoherent flu. As discussed by Nash et al. (2012) and Buijsman et al. (2017), these cross-terms are usually negligible when averaged for a certain time period $[t_1, t_2]$ such as the annual mean. They are not for instantaneous snapshots or monthly averages.

2.3 Other Data

2.3.1 CARS climatology and merged Argo-CARS velocity product

The model used in this study is being evaluated using climatology and observations. Model stratification and water masses vertical structure are evaluated using climatological hydrography data taken from the CSIRO Atlas of Regional Seas (CARS2009) that provides gridded maps of temperature and salinity by combining a variety of datasets (Ridgway et al., 2002, http://www.marine.csiro.au/~dunn/cars2009/). The large-scale regional mean circulation in the Coral Sea is compared to the Argo-CARS merged velocity product from Kessler and Cravatte (2013). This product derives absolute geostrophic currents using climatological hydrographic data from CARS2009 referenced to a level of known motion of 1000 m obtained by drifting trajectories from Argo floats.

2.3.2 Altimetry-derived EKE

Mesoscale eddy kinetic energy (EKE) levels during the period 2014-2018 are evaluated using global ocean gridded maps (1/4°) of SSH generated and processed by the E.U. Copernicus Marine Environment Monitoring Service (CMEMS, https://doi.org/10.48670/moi-00148). In detail, we use the multimission Data Unification and Altimeter Combination System (DUACS) product in delayed time and daily resolution with all satellite missions available at a given time. Mesoscale EKE was computed from

the geostrophic velocity field computed via:

$$EKE = \frac{1}{2} \overline{u'^2_g + v'^2_g},$$ (20)

where

$$u_g = -\frac{g}{f}\frac{\partial \eta}{dy},$$ (21)

$$v_g = \frac{g}{f}\frac{\partial \eta}{dx},$$ (22)

with f the Coriolis parameter, η the SSH above geoid (also referred to as absolute dynamic topography), and

$$(u'_g, v'_g) = (u_g - \overline{u_g}, v_g - \overline{v_g}),$$ (23)

where the overbar denotes the temporal average over the period 2014-2018. Additionally, the geostrophic velocities were high-pass filtered at a cut-off period of 180 days to account for the mesoscale (Qiu and Chen, 2004). We computed the modeled EKE as closely as possible to the altimetric EKE.

2.3.3 In-situ mooring

As part of an assessment of the SARAL/altiKa satellite altimeter for the monitoring of the East Caledonian Current flowing along the Loyalty ridge, moorings and gliders have been deployed along the satellite ground track (Durand et al., 2017). Here, we take advantage of the current-meter mooring at 167.26° E, 20.44° W (about 30 km off the northern tip of Lifou Island in the core of the ECC; see Fig. 3a). The mooring was deployed from November 2010 to October 2011 at the bottom of the continental slope, in 3300 m water depth. It was equipped with an upward-looking LinkQuest FlowQuest 300 kHz ADCP (with 4 m bins) located at a mean depth of 80 m, and five RCM7 Aanderaa rotor current meters at 300, 400, 500, 600, and 1000 m. The mooring provided hourly records of the 1-min averaged ocean velocity over the upper 1000 m. Here, it is used to compare in-situ kinetic energy with the model (cf Sect. 3.3)

2.3.4 FES2014

The FES2014 global ocean tidal atlas (Lyard et al., 2021) is the latest release to improve tidal predictions based on the hydrodynamic modeling of tides (Toulouse Unstructured Grid Ocean model, further denoted T-UGOm) coupled to an ensemble data assimilation code (spectral ensemble optimal interpolation, denoted SpEnOI). It is a very significant upgrade compared to the previous atlases, thanks to the improvement of the assimilated data accuracy and the model performance. FES2014 has been integrated in satellite altimetry geophysical data records (GDRs). It also provides very accurate open-boundary tidal conditions for regional and coastal modeling. Here, it is used to ensure the correct representation of the barotropic tide for SSH in both the host and nesting grid.

2.3.5 HRET

The expression of internal tides in SSH in our model simulation is evaluated by the High Resolution Empirical Tide version 8.1 (HRET8.1, https://ingria.ceoas.oregonstate.edu/~zarone/downloads.html, Zaron, 2019; Carrere et al., 2021). The product uses

305 essentially all exact-repeat altimeter mission data in the period 1992-2017 (TOPEX/Jason, Geosat, ERS, Envisat). In contrast to other previous approaches, HRET differs by the subtraction of the mesoscale sea level anomaly from the SSH along the ground tracks. This ensures to have as little non-tidal variability as possible. This is followed by a harmonic analysis applied on a time series at each point along the ground track for missions with the same orbit. Eventually, HRET distinguishes from other products by being purely empirical. This stands in contrast with the models from Ray and Zaron (2016), Dushaw (2015),

310 and Zhao et al. (2016) that obey dynamical hypothesis such as linear dynamics, spatial coherence, and the usage of a dispersion relation for internal waves at tidal frequency.

2.3.6 Semi-analytical models

Semi-analytical models have been developed to obtain a global estimate of energy conversion rates from the barotropic to the baroclinic tide using bottom topography, climatological stratification, and tidal barotropic velocity (e.g. Nycander, 2005; Fala-

315 hat et al., 2014; Vic et al., 2019). In contrast to high-resolution numerical simulations, they require relatively low computational expenses. Further, they are highly valuable for tidal mixing parameterizations in ocean and climate models that do not have the ability to explicitly resolve tidal processes (MacKinnon et al., 2017; de Lavergne et al., 2019, 2020). Decomposed into vertical modes, the semi-analytical models from Falahat et al. (2014) and Vic et al. (2019), however, rely on strong assumptions which are based on previous findings using linear theory (Bell Jr, 1975; Smith and Young, 2002). First, tidal conversion occurs only

320 over bathymetric slopes that are smaller than the internal tide wave slopes, i.e. subcritical slopes. The wave ray-path slope s is obtained from the dispersion relation as follows:

$$s = \sqrt{\frac{\omega^2 - f^2}{N^2 - \omega^2}},\tag{24}$$

where ω is the eigenfrequency. The buoyancy frequency N is taken from near the ocean bottom. The steepness parameter α, defined as the ratio of the seafloor topographic slope to the ray-path slope, qualifies the seafloor topography as subcritical,

325 critical, and supercritical. Following de Lavergne et al. (2019), we categorize the topographic slopes as stated below:

$$\alpha < 0.8 \, s \quad \text{(subcritical)},\tag{25}$$
$$0.8 \, s < \alpha < 1.5 \, s \quad \text{(critical)},\tag{26}$$
$$\alpha > 1.5 \, s \quad \text{(supercritical)}\tag{27}$$

Conversion in semi-analytical models on critical to supercritical slopes may feature unrealistic values, e.g. conversion larger

330 than the energy lost by the barotropic tide, due to the violation of linear theory. Therefore, a correction for conversion on supercritical slopes is applied in the products of Falahat et al. (2014) and Vic et al. (2019).

Second, horizontal tidal excursion ($\mathbf{U}/w$) is assumed to be smaller than the horizontal topographic scale (Falahat et al., 2014).

This is true for large topographic features (e.g. mid-ocean ridges) and in the deep ocean where barotropic velocities are small. However, in shallow waters (e.g. continental slopes, shelf breaks) this assumption may be violated due to elevated barotropic

335 velocities. For this reason, conversion is usually discarded in the upper ocean. For instance, Falahat et al. (2014) and Vic et al. (2019) do not consider conversions in the upper 400 m and 700 m, respectively. At the same time, this ensures that critical to supercritical slopes which result from increasing stratification in shallower water (through the wave ray-path slope relationship in Eq. 24) are excluded.

Third, it is assumed that the bathymetric height is small relative to the vertical scale of the wave. This is also known as the

340 weak topography approximation (Smith and Young, 2002).

3 Model assessment

The circulation in the Coral Sea is highly constrained by bathymetric features; the generation of internal tides is also closely related to the bathymetry encountered by the barotropic tidal currents. We start here with a description of the characteristics of the topography of the regional model domain (Fig. 1b). The Coral Sea around New Caledonia features a complex northwest-

345 southeast extending ridge system, deep-reaching trenches, small-scale basins, seamounts, and shallow lagoons. The ridge system is composed of two major ridges, the Norfolk and Loyalty Ridge. The Norfolk Ridge extends from north of the Grand Passage all the way to the northern tip of New Zealand. The main New Caledonia island (Grande Terre) is located on the northern segment of the Norfolk Ridge, also referred to as the New Caledonia Ridge. The Loyalty Ridge stretches parallel to the Norfolk Ridge giving rise to the Loyalty Islands (Payri and de Forges, 2006). Seamounts are ubiquitous around New

350 Caledonia, most prominent south of Grand Terre (Samadi et al., 2006).

3.1 Mean circulation

A correct representation of the regional circulation is essential to describe the interaction between the internal tide field and background flow around New Caledonia. The main feature is a westward inflow of waters from the South Pacific Subtropical Gyre which splits up into strong zonal jets, western boundary currents, and eastward counter currents when encountering

355 bathymetric features (Couvelard, 2007; Kessler and Cravatte, 2013; Cravatte et al., 2015; Qiu and Chen, 2004). The 2014-2018 mean, near surface (20-100 m) simulated velocity field (Fig. 2a) is compared to the Argo-CARS merged velocity (see Sect. 2.3.1 for a description, Fig. 2b). The model 5-year mean shows good agreement with the observed regional circulation. The westward zonal jets are well represented with the South Equatorial Current (SEC) being split up into the North Vanuatu Jet (NVJ) and the North Caledonian Jet (NCJ) north of New Caledonia and the South Caledonian Jet (SCJ) south of New

360 Caledonia. West of the main islands (New Caledonia, Vanuatu, Fiji), the observed surface eastward counter currents (Qiu et al., 2009) are also well simulated. The circulation south of New Caledonia seems overall more variable, with less clearly defined mean currents in both products. There is evidence for the presence of the surface-intensified eastward Subtropical Counter Current (STCC) that emerges from the East Australian Current (EAC) recirculation (Ridgway and Dunn, 2003). It is clearly

intensified in the model but the Argo-merged product south of New Caledonia should be taken with caution since limited
365 observations do not average out the signatures of ubiquitous mesoscale eddies.

3.2 Mesoscale variability

The large-scale circulation around New Caledonia is subject to barotropic and baroclinic instability through horizontally and
vertically sheared currents (Qiu and Chen, 2004; Qiu et al., 2008, 2009) giving rise to mesoscale eddy variability. Here, the
spatial pattern of the surface model mesoscale EKE (Fig. 3a) is compared to the mesoscale EKE as observed by satellite
370 altimetry (Fig. 3b). We computed the modeled EKE as closely as possible to the altimetric EKE. To do so, we computed the 5-
day mean of the model SSH to eliminate high-frequency variability such as tidal and inertial motion before horizontally binning
the data onto the grid of present-day altimetry (1/4°). For proper comparison between model and altimeter observations, we
also compute the 5-day average for altimetric SSH before the derivation of mesoscale EKE. Mesoscale EKE is maximum south
of New Caledonia where mesoscale activity is expected through baroclinic instabilities of the vertically sheared SEC/SCJ-
375 STCC currents (Qiu et al., 2009; Keppler et al., 2018). Elevated levels of EKE are also found along the eastern boundary
current system between New Caledonia and Vanuatu and in the northwest of the domain through horizontal shear between
the westward NCJ and the eastward Coral Sea Counter Current (Fig. 2, Fig. 3a). The spatial pattern of simulated EKE is in
good agreement with satellite altimetry (Fig. 3b). Maximum levels of EKE in the southern domain where mesoscale activity
is high are essentially lower than in the model (> 250 cm^2 s^{-2} compared to > 400 cm^2 s^{-2}). We argue that this attributed to
380 the present-day 2-dimensional satellite altimetry products. They are derived by gridding and optimal interpolation of available
along-track SSH data, projected onto a 1/4°horizontal grid, and do not resolve wavelengths smaller than 150-200 km in our
study region (Ballarotta et al., 2019). The model, even though gridded to 1/4°resolution, might contain dynamics that are
associated with smaller scales.

3.3 Kinetic energy frequency spectra

385 In-situ observations are also used to validate energy levels from seasonal down to tidal frequencies obtained from a full-year
in-situ current meter mooring (cf Sect. 2.3.3, Fig. 4). Model energy levels are very close to observations from seasonal to
inertial timescales (180 days to 36 hours), i.e. for meso- and submesoscale processes. Inertial and tidal energy peaks are also
in good agreement. For higher frequencies, the simulation with tidal forcing (red line) introduces a major improvement to the
simulation without tidal forcing (blue line). This is especially true for the internal wave continuum raising the energy levels
390 closer to the observations for frequencies $< f$. This validation, even if only performed at one location, gives us confidence in
the ability of the numerical simulation to correctly represent the tides and their interaction with mesoscale processes.

3.4 Barotropic-baroclinic M2 tide validation

The barotropic tide in both the host grid (TROPICO12) and the nesting grid (CALEDO60) is compared with the empirical
estimates from the barotropic tide model FES2014 (cf Sect. 2.3.4) by applying a harmonic analysis on the full-model hourly

395   SSH. Note that the output from TROPICO12 does not allow for a decomposition between the barotropic and baroclinic tide through the projection onto vertical modes. Therefore, we treat the full-model SSH as a proxy for the barotropic tide. For the sake of consistency, we do similarly for CALEDO60. The M2 tide of TROPICO12 (Fig. 5a) and CALEDO60 (Fig. 5c) are in overall accordance with FES2014 (Fig. 5c and Fig. 5d, respectively). The amphidromic points are well located and amplitudes of SSH are of the same order of magnitude.

400   The baroclinic signature in SSH that expresses in the modulations at shorter wavelengths while distorting the barotropic tide field is evident from Fig. 5c. The baroclinic tide (internal tide) introduced above has generally smaller signatures in SSH and smaller horizontal scales. The baroclinic M2 tide SSH signature obtained from the barotropic/baroclinic decomposition for CALEDO60 (cf Sect. 2.2.1) is shown in Fig. 5e with SSH amplitudes of locally more than 6 cm north and south of New Caledonia. It is in good agreement with the satellite altimetry derived empirical estimates from the HRET model (cf Sect.

405   2.3.5, Fig. 5f). Even though amplitudes appear to be enhanced in our simulation, the spatial representation of the M2 tide is comparable with altimetry. A reasonable explanation for the given differences may be associated with the different time periods the datasets are referenced to as well as the length of the time series for the model (1 year) and altimetry (25 years). This was recently shown by Buijsman et al. (2020) that highlighted decreasing variance of the stationary tide signal with increasing duration of the time series. Overall, we argue that the barotropic and baroclinic tide is well represented in the model

410   suggesting a proper wave propagation from the initial tide forcing and into the nesting grid with no inconsistencies at the nesting boundaries.

3.5 Stratification

Finally, in order to properly study internal tide dynamics, a correct representation of the ocean's stratification is essential. Internal tide express inter alia in the vertical displacement of isopycnal surfaces (Arbic et al., 2018) which can be decomposed

415   by a sum of discrete baroclinic modes that only depend on buoyancy frequency and water depth (cd Sect. 2.2.1). We compare the vertical hydrographic structure of CALEDO60 with a hydrographic climatology (CARS2009, cf Sect. 2.3.1). The model mean density was horizontally binned to the climatological grid (1/2°), whereas the climatological density was vertically interpolated onto the model grid. The water masses (not shown) and buoyancy frequency profiles correspond well with each other. An example of such comparison is illustrated by looking at a stratification profile south of New Caledonia (166° E, 26° S,

420   Fig. 6a). The maximum stratification around 100 m depth is slightly reduced in the model compared to climatology. This is attributed to a reduced salinity maximum in the thermocline in the model (not shown). The normalized modal structures for the four lowest modes and for both the displacement and vertical velocity (Fig. 6b) agree well with climatology. In particular, the depths of the zero-crossing correspond well with each other.

Overall, we conclude that our model simulation is capable of realistically simulating both background ocean dynamics and

425   internal tides. This encourages us to study in detail the internal tide field around New Caledonia including its tidal energy budget, its vertical structure, its interaction with the background currents, and finally its signature in SSH.

4 Barotropic-baroclinic M2 tide energy budget

In the following, we first analyze the M2 internal tide field around New Caledonia by quantifying the energy conversion from the barotropic to the baroclinic tide. We also discuss the overall energy budget of the coherent M2 internal tide. We start with
430   the full-domain before focusing on regional hot spots of internal tide generation.

4.1   Regional overview

The M2 barotropic-to-baroclinic conversion and the barotropic energy flux are shown in Fig. 7a for the full model domain. Positive conversions represent energy transfer from the barotropic to the baroclinic tide; negative conversion are argued to be a measure of the energy transfer from the baroclinic tide to the barotropic tide due to pressure work (Zilberman et al., 2009).
435   However, they may also reflect limitations in the baroclinic/barotropic decomposition (Lahaye et al., 2020). Thus, they remain difficult to explain physically and will not be further discussed here.

In the full-model domain, a total 21.16 GW of barotropic tidal energy is lost of which 72 % (15.27 GW) is transferred to baroclinic tidal energy, whereas 28 % (5.89 GW) is dissipated due to bottom friction. This is a significant loss of barotropic tidal energy. For comparison, barotropic tidal energy loss has been estimated at 18.35 GW and 2.73 GW of which 94 % and
440   84 % are converted to baroclinic tidal energy for the Luzon Strait (Kerry et al., 2013) and the Hawaiian Ridge (Carter et al., 2008), respectively.

Tidal energy conversion is closely linked to bathymetry features as the barotropic tidal flux encounters continental slopes, ridges, and seamounts when it curves southwestward around the New Caledonian ridge system (Fig. 1b, Fig. 7a). In the whole domain (not shown), conversion is observed at all depths up to 4000 m and over a broad range of slopes. However, tidal
445   conversion peaks in shallow waters with overall 25 % of the area-integrated energy that is associated with the upper 500 m. Moreover, two-thirds of the tidal conversion occurs on critical and supercritical slopes. Low vertical modes (mode-1) clearly dominate, explaining almost 70 % of the total tidal energy conversion. Higher modes play only a minor role (15 % for mode-2, and 7 % for mode-3). For the whole domain, 93 % of this generated baroclinic energy is finally dissipated inside the domain, while only little energy (1.06 GW) is leaving the domain (Fig. 7a). Note that this quantity is representative for the net baroclinic
450   flux of inward and outward energy propagation.

4.2   Sub-regional analyses

A large part of the full-domain energy conversion is, in fact, confined to four regions around New Caledonia that represent roughly 60 % of the full-domain area-integrated M2 barotropic-to-baroclinic conversion. These four regions, hot spots of internal tide generation, are illustrated by the black boxes in Fig. 1b-c and Fig. 7a and defined as *North* (1), *South* (2), *Norfolk*
455   *Ridge* (3), and *Loyalty Ridge* (4). The conversion and energy budget are discussed for each area in the light of its topographic characteristics (Fig. 1b-c). The energy budget and the part dissipated locally is also provided for each subregion to better infer where the dissipation occurs and where tidal mixing is expected (Fig. 8, see also Table A1).

The *North* (1) domain is characterized by a very steep (with critical and supercritical slopes) shelf break at the eastern flank of

the New Caledonia Ridge and a 500 m deep, 50 km wide passage (Grand Passage) that is located between the d'Entrecasteaux
460 Reef and the main island reef (Fig. 1b-c). Two-thirds of the tidal energy conversion occurs at depths shallower than 500 m (Fig.
7b), predominantly on critical and supercritical slopes (Fig. 1c). The region features the highest dissipation rate of barotropic
energy. Of 3.83 GW that is lost by the barotropic tide, 1.66 GW (43 %) is directly lost through bottom friction (Fig. 8a, Table
A1). Of the 2.17 GW that is converted to baroclinic energy, 32 % (0.70 GW) dissipates locally while the remaining 68 %
(1.47 GW) radiates away.

465 The *South* (2) domain has similar bathymetric characteristics in terms of depth and slopes. It represents the southward extension
of the New Caledonia Ridge, just south of the New Caledonian lagoon. The most prominent bathymetric feature is the Pines
Ridge: it is a very steep (critical and supercritical slopes) and narrow ridge (a few tens of km wide) of 100 km length that may
be as shallow as 500 m. Orientated perpendicularly to the barotropic tidal flux, it is of great importance for the local internal
tide generation. The *South* (2) domain is also characterized by the presence of a second parallel ridge and of several isolated
470 seamounts, as shallow as 50 m. In this region, half of the tidal energy conversion occurs at depths shallower than 500 m (Fig.
7c), predominantly on critical and supercritical slopes found near the Pines Ridge (Fig. 1c). The *South* (2) domain is subject to
the most-intense energy conversion with a total of 3.92 GW (Fig. 8b, Table A1). It contributes by more than 40 % to the total
conversion associated with the four subregions. Local dissipation is essentially higher than in the *North* (1) domain accounting
for 53 % (2.09 GW), whereas only 47 % (1.83 GW) radiates outside the domain.

475 The *Norfolk Ridge* (3) exhibits different bathymetric characteristics. It is defined as the > 100 km wide north-south stretching
ridge between 24.5° S and 28.5° S. It is dominated by subcritical slopes at depths > 1000 m (Fig. 1c), and also features steep
(critical) slopes at mid-depths (400-700 m) which are mostly associated with seamounts. It is mainly characterized by energy
conversion at subcritical slopes peaking at depths in the range 1000-2000 m with the 50th % percentile at around 1500 m and
the 90th % percentile below 2000 m (Fig. 7d). Similarly to *South* (2), approximately half (53 %) of the converted baroclinic
480 energy (2.04 GW) is dissipated locally (1.07 GW) with the other half (47 %) being radiated away (0.96 GW, Fig. 8c, Table
A1).

The *Loyalty Ridge* (4) is a deep and narrow ridge composed of seamounts and guyots (Pelletier, 2007). These seamounts and
guyots are located between 1000-2000 m depth but deeper ones are also found between 2500-3000 m. They are characterized by
supercritical and critical slopes, respectively. It features the most efficient energy conversion from the barotropic to baroclinic
485 tide. Of 1.28 GW that is lost by the barotropic tide, only 0.31 GW (24 %) is directly lost through bottom friction (Fig. 8d, Table
A1). The area-integrated baroclinic energy accounts for 0.97 GW of which 45 % dissipates within the region (0.44 GW) and
55 % leaves the domain (0.53 GW).

Most of the tidal energy conversion discussed above is dominated by mode-1 explaining 75 %, 84 %, 76 % for *North* (1),
South (2), and *Norfolk Ridge* (3), respectively (Fig. 8a-c, Table A1). In these, regions, mode-2 (7-12 %) and mode-3 (4-6 %)
490 contribute only little to the total baroclinic energy conversion. The *Loyalty Ridge* (4) represents an exception with notable
contributions of higher vertical modes: 43 %, 31 %, 11 %, and 6 % associated with mode-1 through mode-4, respectively (Fig.
8d, Table A1).

These findings are partly consistent with previous conclusions. In shallow depth ranges, the tidal energy conversion is expected

to be largest for mode-1 (Falahat et al., 2014). Also, we expect mode-1 to be dominant for steep, tall, narrow structures such
495 as in the *North* (1) and *South* (2) domains, similarly found for the Hawaiian Ridge (Laurent et al., 2003; Laurent and Nash,
2004). In case of a deeper ocean bottom with small-scale bathymetric structures, such as the *Loyalty Ridge* (4), higher modes
are expected to become more important. The general presence of critical and subcritical slopes suggests a superposition of
numerous vertical modes forming beams. Nevertheless, we did not find any clear relationship between the bathymetric slope
and excitement of vertical modes. The high dissipation rates in *South* (2) and *Norfolk Ridge* (3) could be explained by the
500 successive bathymetric obstacles encountered by the internal tide beams emanating from the generation spots with low modes
scattered to higher modes before being dissipated locally (Lahaye et al., 2020). Surprisingly, the fraction of energy dissipation
around *Loyalty Ridge* is slightly reduced even though higher vertical modes are generated, which should imply more local
dissipation.

4.3 Comparison with semi-analytical model estimates

505 In the following, we compare our M2 conversion rates with semi-analytical model estimates from Falahat et al. (2014) and
Vic et al. (2019) (cf Sect. 2.3.6). Modal energy conversion for the M2 tide is compared in Fig. 9 for the four subregions to the
semi-analytical model estimates.

Overall, there is good agreement between our model estimates and those from semi-analytical theory. This concerns the correct
reproduction of mode-1 dominance and the modal distribution of the area-integrated conversion. Differences are most evident
510 in the *North* (1) (Fig. 9a) and the *South* (2) (Fig. 9b) domains. Part of the discrepancies may be attributed to the featured
bathymetric products that differ in both horizontal resolution and the correct representation of the bathymetric structures. These
two regions may be largely affected by the linear assumptions made in semi-analytical theory (see Sect. 2.3.6 for more details).
As shown in Sect. 4.2, up to 50 % of the tidal energy conversion occurs in waters as shallow as 500 m and above supercritical
slopes. Conversion in such shallow waters is usually discarded in semi-analytical models, explaining the mismatch between
515 the numerical and semi-analytical conversion estimates in the *North* (1) (Fig. 9a) and the *South* (2) (Fig. 9b) domains.

Conversion estimates compare better for those regions where slopes are mostly subcritical (such as *Norfolk Ridge* (3)) or where
conversion occurs deeper (such as *Loyalty Ridge* (4)). In the latter, the contribution of higher modes is also well represented.
While semi-analytical theory has proven very valuable in providing a first-order estimation of internal tide generation on
global scales, we highlight here the need for realistic, high-resolution numerical simulations to more faithfully represent the
520 local internal tide generation and dynamics. This is especially true in regions such as New Caledonia with shallow and complex
bathymetry with critical to supercritical slopes, for which semi-analytical models reach their limits.

4.4 Zoom in the *South* (2) domain

The *South* (2) domain deserves special attention for two reasons: First, it is of particular importance since it represents a study
area of the upcoming SWOT-AdAC program accompanied by an extensive field campaign. This will be shortly discussed later
525 in Sec. 7. Second, it represents the predominant hot spot of internal tide generation contributing by more than 25 % to the
full-domain area-integrated barotropic-to-baroclinic energy conversion (Fig. 7a, Fig. 8b).

The M2 barotropic-to-baroclinic energy conversion and dissipation is explicitly shown in Fig. 10 indicating the incoming and outgoing barotropic and baroclinic energy flux integrated along the respective boundaries. In total, 6.16 GW are lost by the barotropic tide of which 64 % (3.92 GW) are converted to internal tides, whereas 2.24 GW are lost through bottom friction

530 (Figure 10a). Figure 10a reveals several distinct hot spots of conversion. Internal tides are mainly formed along and on both sides of the Pines Ridge, the southward extension of the New Caledonia Ridge. It represents a major obstacle for the barotropic tidal flow and is associated with high conversion rates well above 1 W m^{-2} (locally > 5 W m^{-2}) on both its western and eastern flanks. Further internal tide generation is localized downstream along a secondary ridge parallel to the Pines Ridge and across the western shelf break. Locally, positive conversion is also evident around seamounts that are present in the area, namely,

535 Munida, Antigonia, Jumeux Est, and Stylaster. There could be some resonance or interference patterns that are responsible for negative values. In contrast to the conversion map which shows isolated spots, dissipation is observed throughout the domain (Fig. 10b). Integrated over the domain, baroclinic energy dissipation accounts for over half of the converted energy (53 %, Fig. 10b). Dissipation maxima are located near the generations sites such as Pines Ridge and around the semaounts with dissipation rates of > 0.5 W m^{-2}, i.e. around Munida, Brachiopode, Jumeux Ouest, and Stylaster. Increased levels of dissipation are also

540 found along the barrier reef that encloses the South Caledonian lagoon. Further energy dissipation occurs uniformly westward and eastward of the Pines Ridge across the shelf break with constant dissipation rates of about > 0.1 W m^{-2}.

Our model results show that the fraction of internal tides that dissipate locally ($q = D_{bc}/C$) is elevated in our study area (~50 %) compared to 36 % and 20 % for the Luzon Strait (Kerry et al., 2013) and the Hawaiian Ridge (Carter et al., 2008), respectively. Given the high-dominance of mode-1 (Fig. 8), one would expect a small fraction of locally dissipated energy. Sev-

545 eral processes of tidal energy dissipation have been discussed in literature, well summarized in de Lavergne et al. (2019, 2020): non-linear wave-wave interactions, wave breaking through shoaling, dissipation on critical slopes, and scattering by abyssal hills. The wave-wave interactions concern only higher modes since low modes are characterized by slow rates of attenuation due to high group speeds (Nikurashin and Legg, 2011; Olbers et al., 2020), whereas the dissipation of low-mode internal tides is rather affected by the interaction with topography (Kelly et al., 2013). However, we suggest that the high fraction of

550 local energy dissipation (q = 0.5) could be related to the interaction with the complex topography such as small-scale ridges, seamounts, and subcritical to critical slopes in along-beam (downstream) direction causing scattering/energy transfer of the low-mode internal tide to higher modes and shoaling close to the New Caledonian barrier reef (Lahaye et al., 2020).

The non-dissipated energy propagates away from the main generation site within a tidal beam characterized by energy fluxes of 20 kW m^{-1} (and up to 30 kW m^{-1}) which in turn attenuate gradually to 10 kW m^{-1} within 100 km distance to the generation

555 site. The baroclinic energy flux diverges at the Pines Ridge while propagating in southwestern and northeastern direction with a net energy flux of 1.83 GW leaving the domain. This accounts for 47 % of the locally generated baroclinic tidal energy.

5 Tidal energy flux and loss of coherence

In the following, we address the temporal and spatial variability of the semidiurnal internal tide by decomposing the energy
flux into coherent and incoherent parts (see methodology presented in Sect. 2.2.3). The annual mean of the total, coherent, and
incoherent semidiurnal energy flux is shown for the full CALEDO60 domain in Fig. 11, where the incoherent internal tide is
presented as the ratio to the total semidiurnal energy flux. Note that we masked regions in Fig. 11c where the total semidiurnal
energy flux does not exceed 1 kW m^{-1}. The semidiurnal internal tide energy flux is characterized by two predominant tidal
beams that emerge from the *North* (1) and *South* (2) domains. They are 100-200 km in width, feature magnitudes of up to
30 kW m^{-1} near the respective generation sites, but propagate not more than 800 km toward the open ocean. In contrast to the
southern tidal beam that propagates from its formation site at the Pines Ridge southwestward and northeastward (though the
northeastward beam is more limited), the northern tidal beam mainly propagates northeastward. This is attributed to the energy
conversion that is confined to the shelf break east of the Grand Passage, whereas the Grand Passage itself is subject to only
minor energy conversion (not shown). Tidal beams also emerge from the *Norfolk Ridge* (3) and *Loyalty Ridge* (4). However,
they are overall less pronounced and smaller in magnitude (5-10 kW m^{-1}). Similarly to the *North* (1) and *South* (2) domains,
energy of this first mode dissipates quite rapidly, and does not propagate far away from the generation site. Again, this could
be related to the complex topography. With multiple generation sites, it is most likely that wave-wave interactions, topographic
scattering to higher modes, or interaction with critical slopes contribute greatly to the fast energy dissipation.

In the annual mean, the semidiurnal internal tide field is to a large part coherent (Fig. 11b). The incoherent tide gradually
increases in importance with increasing distance to the generation site (Fig. 11c-d). Figure 11c clearly shows that the north-
eastward tidal beams emerging from the *North* (1) and *South* (2) domains remain largely coherent. This is not the case for
the tidal beams emanating from *Norfolk Ridge* (3) and *Loyalty Ridge* (4), and for the southwestward propagating tidal beam
emerging from the *South* (2) domain. Within the latter beam, the incoherent part explains about 25 % of the total semidiurnal
signal beyond 200 km distance to the generation site at Pines Ridge (0 km), before being dominant at > 500 km distance (Fig.
11d).

Here, we attribute the departure from coherence to mesoscale eddy variability. Mesoscale activity is generally increased south
of New Caledonia (Fig. 3) related to an equatorward regime shift from non-linear to more linear dynamics as reported by Kep-
pler et al. (2018). We argue that incoherent tidal energy levels depend largely on the local eddy activity: it is in accordance with
Fig. 11c, where the incoherent tide is of higher importance in the southern half of the domain. This is exemplarily shown by a
5-day snaphot (31 January 2014) of the incoherent semidiurnal energy flux overlaid by the mesoscale circulation in Fig. 12a.
In the influence area of the tidal beams, elevated incoherent energy levels are clearly linked with intensified mesoscale currents
associated with large SSH gradients. Tidal energy flux becomes incoherent as it propagates through an eddy field. It can also
be related to temporal variability of the conversion term at the internal tide generation site associated with local changes of
stratification (expressed by pressure amplitude variations) or remotely generated internal tides (expressed by pressure phase
variations) as previously reported by Zilberman et al. (2011) and Kerry et al. (2014, 2016). To assess the temporal variability
of the conversion term, we divide the full-model calendar year into monthly datasets and apply the tidal analysis as described

in Sect. 2.2.1 to obtain an estimation of the month-to-month evolution. We focus on the four generation zones and consider only locations with a conversion > 0.1 W m^{-2} associated with the internal tide generation hot spots.

The corresponding monthly normalized standard deviation of the area-integrated conversion (not shown) is globally rather low ranging from 5-8 % with *North* (1) and *South* (2) domains to 9-14 % within *Norfolk Ridge* (3) and *Loyalty Ridge* (4). However, it can be much higher locally, potentially reaching 100 %. This is evident from the spatial maps of conversion variability that are shown for each subregion in Fig. 13. They reveal locations of high variability, i.e. near small-scale bathymetric structures. Here, the month-to-month variability of the local conversion term appears to be largely governed by pressure amplitude variations, especially in the *North* (1) and *South* (2) domains (illustrated by the hatched contours in Fig. 13), suggesting that local stratification effects dominate. Variations of the phase differences tend to be enhanced in the *Norfolk Ridge* (3) suggesting that remotely generated incoherent tides effects dominate.

Variations of pressure amplitude and phase during the year do not follow a seasonal cycle. Rather, as for the energy flux, we suggest that stratification changes and associated pressure amplitude variations are linked with mesoscale eddy variability. An illustration is given by the conversion anomaly for April 2014 overlaid by a representative snapshot of the mesoscale circulation (26 April 2014) in Fig. 12b. The negative conversion anomaly around Pines Ridge governed by baroclinic pressure amplitude variations clearly coincides with the passage of a mesoscale eddy which remains in the region for almost the entirety of the month expressed by elevated levels of EKE (inset of Fig. 12b). This leads to a temporal decrease of tidal energy conversion and consequently a decline in baroclinic energy flux divergence. We conclude that the conversion term is relatively constant over time, but some sporadic event like eddies close to the generation site may temporally influence it.

6 Internal tide SSH signature

Finally, we address the SSH signature of internal tides. We first investigate the SSH amplitude of the semidiurnal internal tide and its spatial distribution around New Caledonia before addressing its wavenumber spectral signature in relation with SWOT observability. The questions of interest for SWOT observability are: What are the processes (high-frequency signals, low-frequency signals) that dominate in our study region the SSH signal in the meso- to submesoscale range? What are the contributions of internal tides to these SSH signals and does the coherent or incoherent part dominate? What is the associated transition scale between balanced and unbalanced motions? Once the coherent tide SSH signal has been removed from the total SSH signal, what will SWOT be able to observe? How does the correction of the coherent SSH signal modify the transition scale?

6.1 SSH amplitude of the semidiurnal internal tide around New Caledonia

A spatial map of the SSH root-mean-square (rms) of the coherent and incoherent semidiurnal internal tide (relative to the 1-year period) are presented in Fig. 14. For the coherent signal (Fig. 14a), multiple interference SSH patterns clearly highlight the complexity of the area, with semidiurnal tidal waves emanating from multiple generation areas and summing constructively and destructively as they propagate. The coherent semidiurnal internal tide features a rms of more than 6 cm near the internal

tide generation sites in the *North* (1) and *South* (2) domains. The overall signature resembles the semidiurnal energy flux in
Fig. 11b with the predominant tidal beams to the north and south of New Caledonia clearly visible in SSH. The incoherent
semidiurnal internal tide SSH manifestation (Fig. 14b) is characterized by overall smaller rms with a maximum of locally
2 cm. The incoherent SSH is less confined to the tidal beams and it seems overall more widespread both north and south of
New Caledonia. This tidal signature outside the energy flux tidal beams has a rather low rms of 0.5-1 cm, and expresses the
dispersion of internal waves propagating through the domain without explicit energy propagation. This implies that the internal
tide SSH signature is not purely confined in energetic tidal beams. Recall from Sect. 3.4 that we have a robust estimate of
the coherent tide based on altimetric products. Moreover, our model estimates of SSH signature are in good agreement with
altimetry (Fig. 5e-f). However, we suggest that the incoherent tide could introduce a residual error in altimetric measurements
beyond the areas of main tidal energy propagation where internal tides are weaker.

6.2 SSH spectral signature

Wavenumber SSH spectra are commonly used to investigate dynamical regimes at work, and to explore the relative importance
of balanced and unbalanced motion which may feature similar wavelengths: the wavenumber slopes and relative levels of vari-
ance both provide information on these issues (e.g. Le Traon et al., 2008; Dufau et al., 2016; Savage et al., 2017; Tchilibou
et al., 2020, 2022; Vergara et al., 2022, and many more). The observability of meso- and submesoscale dynamics (balanced
motions in this case) is ultimately governed by the transition scale that separates balanced from unbalanced motion and which
was found to vary regionally and seasonally (Qiu et al., 2018). In particular, the transition scale is a quantitative measure to
estimate above which scales in spectral space the geostrophic balance is valid to derive mesoscale dynamics. The objective
here is to describe the altimetry-like and along-track SSH spectra (corrected for the barotropic tide, SSH_alt) with regard to
the different dynamics that are separated in terms of frequency bands: subinertial (f < 1/36 h, SSH_subinertial), superinertial
frequencies (f > 1/36 h, SSH_alt_superinertial) for internal gravity waves by distinguishing between the coherent (SSH_coh)
and incoherent (SSH_inc) total (1/10 h - 1/28 h) tide as well as the supertidal frequencies (f > 1/10 h, SSH_alt_supertidal). The
transition scale is defined here as the intersection of subinertial and superinertial spectra.

In Fig. 15, we compute wavenumber spectra in along-beam direction (as indicated in Fig. 15a) for summer (January-March,
Fig. 15a) and winter (July-September, Fig. 15b) months. Independent of the season and for scales larger than 200 km (large
mesoscale), subinertial processes explain almost all of the SSH variance. For scales smaller than 200 km, SSH variance is
governed by superinertial processes which in turn are largely dominated by the internal tide as discussed below.

Seasonal modulations of the altimetry-like SSH spectra become evident at scales in the range 30-300 km. In summer, it features
a more flattened wavenumber slope in the meso- to submesoscale range with a characteristic wave slope of k^{-2} (Fig. 15a) cor-
responding with superinertial motions (internal wave continuum). In winter, it becomes more continuous being characterized
by a wave slope of k^{-4} Fig. 15b. This is mainly attributed to subinertial motions such as meso- to submesoscale processes that
undergo seasonal variability and are energized in winter (e.g. Callies et al., 2015; Rocha et al., 2016). This was explicitly shown
for New Caledonia by Sérazin et al. (2020) where the authors attributed the increasing importance of mixed layer instabilities
and frontogenesis to more available potential energy in winter months. Superinertial processes dominate subinertial motions

in both seasons at scales below 160-180 km, but are more pronounced in summer. This relates to the decreased levels of SSH variance of subinertial frequencies during that time of the year (Fig. 15a). Contrarily, superinertial motions lose in relative
660 importance because of increasing SSH variance of subinertial processes in winter (Fig. 15b).

Motions at superinertial frequencies progressively take over toward smaller scales until explaining all the SSH variance for wavelengths smaller than 140 km in summer and 30-40 km in winter. Along the tidal beam for scales larger than 50 km, superinertial motions are almost entirely explained by internal tides (coherent tides being dominant over incoherent tides). They clearly express in spectral space with mode 1 and mode 2 at 160 km and 80 km wavelengths, respectively. By definition, the
665 coherent tidal signal is the same in both seasons, whereas the incoherent tidal signal is much stronger in summer at scales smaller than 100 km. This is also true for motions at supertidal frequencies. This is consistent with the findings from Lahaye et al. (2019) who found a surface amplification of mode-2 and higher in summer due to increasing stratification while mode-1 is mostly unchanged. This opposition in phase of the seasonality of both meso- to submesoscale and internal gravity waves lead to a seasonally varying transition scale. It is found at 180 km in summer (Fig. 15a). It is not well defined in winter, where
670 both subinertial and superinertial signals have similar variance in the mesoscale band (100-180 km, Fig. 15b).

Subtracting the coherent internal tide from the SSH measurements may be a promising attempt to disentangle balanced SSH. Corrected for the coherent internal tide, observability in summer improves only slightly from 180 km to 160 km (Fig. 15a). However, in winter observability improves from 180 km to wavelengths in the range 50-80 km (Fig. 15b).

In these 1-dimensional wavenumber spectra, which have been computed within a tidal beam, the internal tide signature is rela-
675 tively well represented. This raises the question, though, of how does the anisotropic internal tide signature affect SSH spectra along an altimetric track, not orientated along a tidal beam? As an example, we look at a ground track which resembles the SWOT nadir track during the fast-sampling phase while crossing the strong energy flux south of New Caledonia (Fig. 15c). Due to the track's orientation perpendicular to the tidal beam's propagation direction, the characteristic internal tide signature in our study area is not properly sampled. Moreover, the correction for the coherent tides increases SWOT observability only
680 marginally. We suggest that this is partly attributed to the dominance of the incoherent tide away from the tidal beam's main propagation direction. Nevertheless, applying a coherent tide correction improves the transition scale from 120 km to 80 km for the given SSH spectra relative to the 1-year period. Such a correction is now available in the altimeter products, and we may expect a similar gain in observability from altimetry assuming that model and altimetric spectra compare well. Here, we look at the most precise SSH altimetric 20 Hz data from Sentinel-3a (courtesy Gourdeau et al. in preparation) and altimetric
685 spectra (from denoised SSH) representative of the satellite ground tracks just south of New Caledonia. Despite their reference period (2014 for the model, 2016-2021 for Sentinel-3a) both altimetric and modeled spectra look very much alike down to 50 km wavelength, well below the expected transition scale at 80 km.

Dominance of unbalanced motion in the meso- to submesoscale band strongly limits SSH observability of geostrophic dynamics in our study region, especially in summer. In other words, SSH observability of mesoscale dynamics is limited to large
690 eddy scales. It is to a large part the incoherent tide and motions at supertidal frequencies at scales < 100 km which eventually determine and challenge SSH altimeter, specifically SWOT, observability of meso- and submesoscale dynamics.

7 Summary and discussion

Prominent topographic structures such as oceanic ridges, continental shelf breaks, seamounts, and island chains give rise to major internal tide formation in large parts of the Pacific Ocean (Niwa and Hibiya, 2001). The majority of recent studies on
695 internal tides focused mainly on two regions: the Luzon Strait (e.g. Niwa and Hibiya, 2004; Alford et al., 2011; Kerry et al., 2013) and the Hawaiian Ridge (e.g. Merrifield and Holloway, 2002; Zaron and Egbert, 2006; Carter et al., 2008). Here, we present for the first time the internal tide dynamics around New Caledonia in the Southwestern Tropical Pacific Ocean, using the output of a dedicated high-resolution regional numerical model. Being subject to strong internal tides and elevated mesoscale eddy activity, New Caledonia represents an area of high interest for the upcoming SWOT altimetry mission to eval-
700 uate observability of meso- and submesoscale dynamics in the presence of unbalanced motion at wavelengths of similar scale. This is primarily true for the SWOT fast-sampling phase, when the satellite will sample every day this region of interest. In this context, a dedicated field campaign (SWOTALIS, March-April 2023) will be carried out in the framework of the CLIVAR AdAC program (Morrow et al., 2019; d'Ovidio et al., 2019). Thanks to a tailored high-resolution modeling strategy, the results we obtained provide new and key information for the region, but also more globally for the understanding of the generation
705 and life cycle of internal tides. We were also able to gain insights into SWOT observability in a challenging region with strong internal tidal waves. These findings are summarized and discussed below.

a) New Caledonia: a hot spot of mode-1 internal tide generation in the Pacific

The regional barotropic and baroclinic energy budget of the dominant M2 tide shows that in the full-model domain, 21.16 GW
710 of the barotropic tidal energy is lost of which 72 % (15.27 GW) is converted into baroclinic tidal energy. The main conversion zones are associated with the most prominent bathymetric structures such as the Grand Passage (2.17 GW) and Pines Ridge (3.92 GW), north and south of New Caledonia, respectively. This confirms that New Caledonia is a hot spot of internal tide generation. The amount of energy converted is comparable to what has been estimated in the Luzon Strait (Kerry et al., 2013) and the Hawaiian Ridge (Carter et al., 2008), taking into account that the exact numbers depend on the size of the domain. The
715 area-integrated M2 conversion is estimated as 15.27 GW around New Caledonia, 16.97 GW in the Luzon Strait, and 2.34 GW along the Hawaiian Ridge. Conversion integrated in the smaller subregions *North* (1) and *South* (2) are similar to the Hawaiian Ridge (2.17 GW and 3.92 GW, respectively). Local conversion rates are of the same order of magnitude (well above 1 W m^{-2}) among all regions. Further, all regions feature similar energy propagating away from the formation site in opposing directions within a well-defined tidal beam. Maximum M2 baroclinic energy fluxes vary from 10 kW m^{-1} at the Hawaiian Ridge, up to
720 30 kW m^{-1} around New Caledonia, and 40 kW m^{-1} at the Luzon Strait.

Interestingly, the New Caledonia region stands out compared to other previously studied regions in terms of modal content. Our modeling results suggest that barotropic tidal energy is converted, overwhelmingly, into baroclinic mode-1 (75 % of the full-domain energy conversion, and up 85 % in the *South* (2) domain). Modes 2-4 represent a comparable amount of energy only at the *Loyalty Ridge* (4) characterized by deep topography. For comparison, this mode-1 conversion percentage was es-
725 timated to be around 30 % at global scale, 35 % for the Pacific basin (Falahat et al., 2014; Vic et al., 2019), 30 %-60 %

around Hawaii (Merrifield and Holloway, 2002; Zilberman et al., 2011), and about 9 % over the Northern Atlantic Ridge (Vic et al., 2018). The reasons behind this strongly dominant mode-1 were not completely understood. A dominance of mode-1 in the western Pacific had been suggested previously with semi-analytical models (Falahat et al., 2014; Vic et al., 2019), but not to that extent. Apart from topographic characteristics such as height, width, and depth (Legg and Huijts, 2006; Falahat

730 et al., 2014), the modal content is argued to be primarily governed by roughness and, thus, by the topography's spectral shape (Laurent and Nash, 2004). On the other hand, it has been observed and argued by many that critical and supercritical slopes are conducive to beam-like patterns, requiring the presence of higher vertical modes. Mode-1 has also been suggested to be dominantly generated in shallow depths (Falahat et al., 2014). Fully understanding the strong dominance of mode-1 in our region characterized by the presence of steep, tall, and shallow ridges with critical and supercritical slopes, and 25 % of the

735 conversion happening above 500m, would require further analyses.

An important lesson learned is that New Caledonia, which features complex bathymetry with critical to supercritical slopes and significant tidal energy conversion in shallow waters (< 500 m), often discarded in semi-analytical theory, is too complex for linear semi-analytical models. Such semi-analytical models, although very useful and widely used to estimate tidal energy conversion, its modal distribution, and tidal mixing (e.g. Falahat et al., 2014; Vic et al., 2019; de Lavergne et al., 2019, 2020),

740 miss a significant part of the conversion in our area. Therefore, our study points out the limitation of these approaches in such complex areas, and highlights the relevance of realistic numerical simulations on regional scales.

b) A hot spot of internal tide dissipation

Our model results suggest elevated ratios (q) between local tidal energy dissipation and generation of ∼ 50 % compared to other

745 internal tide generation hot spots in the Luzon Strait (36 %, Kerry et al., 2013) and the Hawaiian Ridge (20 %, Carter et al., 2008). This is surprising considering the clear dominance of mode-1 in most parts of our nesting model domain. Nonetheless, the elevated levels of local energy dissipation provide an explanation for the relatively low propagation distance of the tidal beam, essentially lower compared to the tidal beams emanating from the Luzon Strait and the Hawaiian Ridge that may propagate several thousands of km toward the open ocean. The governing mechanisms of tidal energy dissipation in our study area

750 remain an open question. Yet, we suggest that the large ratio of local energy dissipation is related to the complex topography that favors scattering/energy transfer of the low-mode internal tide to higher modes leading to increasing dissipation close the generation sites.

Knowledge about local dissipation of tidal energy has important implications for ocean- and climate-scale models that do not resolve mixing processes induced by internal tides. Traditionally, a constant fraction of local energy dissipation of 30 % is

755 assumed (St. Laurent et al., 2002), but it was pointed out that near-field dissipation varies spatially across the global ocean and may be as large as 80 % (Laurent and Nash, 2004; Lefauve et al., 2015; Vic et al., 2019; de Lavergne et al., 2019, 2020). This points out to elevated mixing levels in our region compared to the conventional tidal mixing parameterization used in ocean general circulation models. In NEMO, however, the parameterization from de Lavergne et al. (2019) is now implemented.

c) A great spot for studying interactions between tides and mesoscale eddies

760 Our study highlighted internal tide incoherence in both the near-field and far-field, and suggested it arises from mesoscale

eddy variability. In the near-field, the observed variability was attributed mainly to variations of the barotropic to baroclinic conversion term explained by pressure amplitude variations in the *North* (1) and *South* (2) domains. Along the Hawaiian Ridge, Zilberman et al. (2011) found on the contrary that variations in conversion terms were mainly explained in the perturbation pressure phase, thus, suggesting the influence of remotely generated internal tides. Our results adovate for a greater influence of

765   local changes in stratification, and suggest that these pressure amplitude variations are associated with temporally constrained, elevated levels of mesoscale EKE.

When integrated in regional boxes, increased and decreased energy conversion at different spots compensate and the total conversion variability is rather small, and cannot explain the variability in the energy flux divergence. However, it is worth noting that locally, the conversion variability can reach 100 %. This has important implications for the interpretation of data from

770   moorings that will be deployed during the SWOTALIS cruise along the ridge slopes.

In the far field, when propagating away from the generation sites, the internal tidal beam propagating from the *North* (1) domain remains remarkably coherent. The tidal beam emerging from the *South* (2) domain propagating southwestward within the mesoscale eddy field is being deflected and refracted by mesoscale eddies and becomes rapidly incoherent. Snapshots of the incoherent energy flux suggest that tidal incoherence with magnitudes > 10 kW m^{-1} clearly coincides with the intensified

775   mesoscale currents. Previous studies have investigated the interaction of internal tides with background currents, i.e. mid-latitude and equatorial jets, as well as mesoscale turbulence and eddies causing time variable refraction and deflection of the internal tide (Park and Watts, 2006; Ponte and Klein, 2015; Kelly and Lermusiaux, 2016; Magalhães et al., 2016; Buijsman et al., 2017; Tchilibou et al., 2022; Guo et al., 2023). Most recently, Guo et al. (2023) correlated the refraction of the internal tide with mesoscale-eddy driven phase speed variations. Further, the authors show that the refraction of the internal tidal beam

780   is rather associated with the currents of the mesoscale eddies rather than mesoscale-eddy driven stratification changes. A deeper investigation of the processes at work in our area is planned for a further study.

d) A challenging spot for SWOT observability

The SWOT mission is dedicated to document 2-dimensional fine-scale features down to 15 km wavelength that include both subinertial (meso- to submesoscale dynamics) and superinertial (such as internal tides) frequencies. SWOT observability is

785   dependent on the ability to disentangle these different dynamics. The SWOT science community has been working on different approaches to separate balanced motion from internal tides by the allocation of spectral characteristics to their respective dynamics (Torres et al., 2018) and the integration of other remote sensing data (e.g. sea surface temperature, Ponte et al., 2017). More recently, a joint-estimation algorithm and a deep-learning approach have also been tested with sufficient extraction of the internal tide in a turbulent flow from SSH (Le Guillou et al., 2021; Wang et al., 2022).

790   Here, we use the transition scale that separates the larger scale dominated by balanced geostrophic motions from the smaller scale dominated by the unbalanced wave motions which is defined as the wavelength with equal subinertial and superinertial SSH variance based on a 36-hour filtering method.

Wavenumber spectra of SSH reveal the dominance of unbalanced, rapidly-changing motion, largely governed by the internal tide, in the mesoscale band at spectral wavelengths below 160-200 km. Along the tidal beam, the coherent component of inter-

795   nal tides may dominate the incoherent component at wavelengths down to 50 km. A simple approach consists in the subtraction

of the coherent internal tide signature which in turn is derived from decades-long time series collected from conventional satel-lite altimetry (Zhao et al., 2016; Ray and Zaron, 2016; Ubelmann et al., 2022; Zaron, 2019). Correcting our model for the coherent internal tide, we were able to improve SWOT observability (here measured by the transition scale between subinertial and superinertial motions) in winter from 160 km to 50-80 km. In summer, however, observability increases only marginally

800   due to seasonally weaker subinertial signals, and more elevated levels of incoherent tidal energy which remain in the SSH signal after correction for the coherent tide.

This is partly in accordance with the global analysis from Qiu et al. (2018), where the SSH-derived transition scale may be lowered by up to 60-80 km in the Southwestern Tropical Pacific when removing the coherent tide. The in-situ analysis from Sérazin et al. (2020) reveals a general transition scale as low as 10 km, where divergent motions take over rotational dynamics.

805   However, the authors argue that the internal tide signature might vanish due to the application of an isotropic average of their structure functions over bins.

Our results highlight the anisotropic signature of internal tides. When the satellite track crosses the tidal beam perpendicularly (such as the SWOT swath during the fast-sampling phase), the spectral peaks of internal tides are less evident, and the incoher-ent tide tends to dominate. The efficiency of the coherent tide correction to increase observability in the mesoscale depends on

810   the relative orientation of the satellite tracks compared to that of the tidal beams. It becomes clear that SWOT observability of wavelengths < 150 km ultimately depends on our ability to correct for unbalanced motion. This raises serious concerns about SWOT's ability to observe balanced submesoscale processes in our region. We have no doubt, whatsoever, that SWOT data will contribute to and improve the characterization of the internal tide field.

e) Perspectives of this work

815   This work is a first modeling approach to characterize internal tide dynamics around New Caledonia. Despite the tailored modeling strategy at high-resolution (∼1.7 km grid-box spacing), limitations may be attributed to processes which are not resolved by the model effective resolution (13 km, Soufflet et al., 2016). This certainly affects the internal tide generation and dissipation around small topographic features such as seamounts. A higher resolution near those features could improve the explicit representation of the direct energy cascade, i.e. energy transfer and mixing.

820   The results obtained could also be usefully confronted to in-situ observations. The dedicated in-situ SWOTALIS experiment consisting of multiple field campaigns planned during the SWOT fast-sampling phase will provide the needed observations. Observational platforms such as moorings, repeated hydrographic sections, and long fixed stations spanning several semi-diurnal tidal cycles with microstructure measurements will provide further insight into the internal tide life cycle south of New Caledonia, in combination with the SWOT data. Our simulations will help link the full water column dynamics and the SSH

825   measurements.

Our study also suggested that internal tides in our area are strongly sensitive to the mesoscale field, both at the generation sites and along the propagation. Further analyses to understand the dynamical processes at work are needed, and planned for future studies. In addition, a twin simulation experiment, with the same forcing and parameterizations, but without tidal forcing, has been performed. Comparing both simulations will help understand how tides impact the meso- and submesoscale fields, and

830   the forward and inverse energy cascades among spatial scales.

Finally, this study provided first hints on the internal tides dissipation spatial variability. Yet, the impact of tidally-driven mixing on temperature, other tracer fields, and biological variables in this area of high biodiversity remains to be quantified. It is expected that strong vertical velocities along bathymetric slopes, reefs, and seamounts may influence nutrients inputs into the euphotic layer, primary production, potentially up to high trophic levels and marine fauna (Derville et al., 2020). We hope that
835 our results will pave the way to a better understanding of these processes and ultimately help for marine conservation.

Code availability. The tidal analysis was performed using the COMODO-SIROCCO tools which are developed and maintained by the SIROCCO national service (CNRS/INSU). SIROCCO is funded by INSU and Observatoire Midi-Pyrénées/Université Paul Sabatier and receives project support from CNES, SHOM, IFREMER and ANR.

Author contributions. AB performed the analysis and drafted the manuscript under the supervision of LG and SC. LB and AA performed
840 the numerical simulations. The tidal analysis was performed with help of MT and FL including fruitful discussions with CV. All co-authors reviewed the manuscript and contributed to the writing and final editing.

Competing interests. The authors declare that they have no conflict of interest.

Acknowledgements. This work was performed within the PhD program of AB funded by the Faculty of Science and Engineering, University of Toulouse III - Paul-Sabatier and granted by the doctoral school Geosciences, Astrophysics, Space and Environmental Sciences (SDU2E).
845 LG and SC are funded by the Institut de Recherche pour le Développement (IRD); LB and AA were funded by OceanNext, Grenoble; MT was funded by the Centre National d'Études Spatiale (CNES) and FL was funded by the Centre National de la Recherche Scientifique (CNRS); CV was funded by the Institut français de recherche pour l'exploitation de la mer (IFREMER). This work is a contribution to the joint CNES-NASA project *SWOT in the Tropics* and is supported by the French TOSCA (la Terre, l'Océan, les Surfaces Continentales, l'Atmosphère) program and the French national program LEFE (Les Enveloppes Fluides et l'Environnement). Simulations presented in this
850 study were performed at the Centre Informatique National de l'Enseignement Supérieur (CINES). We thank the MEOM/IGE (MultiscalE Ocean Modeling/Institut des Géosciences de l'Environnement) group to be part of their allocation of computational resources. This study has been partially supported through the grant EUR TESS N°ANR-18-EURE-0018 in the framework of the Programme des Investissements d'Avenir. This study has been conducted using E.U. Copernicus Marine Service Information CMEMS (https://doi.org/10.48670/moi-00148). Climatological hydrography data was obtained from CARS (http://www.marine.csiro.au/~dunn/cars2009/). FES2014 was produced by Nov-
855 eltis, LEGOS, and CLS and distributed by Aviso+, with support from CNES (https://www.aviso.altimetry.fr/). We acknowledge the publicly available HRET products from Edward Zaron (https://ingria.ceoas.oregonstate.edu/~zarone/downloads.html). Figures were created using Python 3.9, Matplotlib 3.5.1, and colormaps provided by Thyng et al. (2016) and van der Velden (2020). We thank Mathilde Cancet for the preparation of the bathymetry dataset and Amélie Ferran for previous work on the modelisation and analysis of internal tides around New Caledonia. Further, we appreciate the fruitful discussions with Jerome Chanut, Julien Le Sommer as well as Ritabrata Thakur and Brian

860   Arbic with helpful comments on the modeling part. Finally, we thank the SWOT Science Teams *High-resolution Ocean Modeling Group* (led by Brian Arbic, Florent Lyard, and Lionel Renault) and *Tides, Internal Tides, and Internal Gravity Waves* (led by Edward Zaron and Brian Arbic) providing a platform for scientific exchanges and discussion.

References

Alford, M. H.: Redistribution of energy available for ocean mixing by long-range propagation of internal waves, Nature, 423, 159–162,
865   https://doi.org/10.1038/nature01628, 2003.

Alford, M. H., MacKinnon, J. A., Nash, J. D., Simmons, H., Pickering, A., Klymak, J. M., Pinkel, R., Sun, O., Rainville, L., Musgrave,
     R., et al.: Energy flux and dissipation in Luzon Strait: Two tales of two ridges, Journal of Physical Oceanography, 41, 2211–2222,
     https://doi.org/10.1175/JPO-D-11-073.1, 2011.

Arbic, B. K., Alford, M. H., Ansong, J. K., Buijsman, M. C., Ciotti, R. B., Farrar, J. T., Hallberg, R. W., Henze, C. E., Hill, C. N., Luecke,
870   C. A., et al.: Primer on global internal tide and internal gravity wave continuum modeling in HYCOM and MITgcm, New frontiers in
     operational oceanography, pp. 307–392, http://purl.flvc.org/fsu/fd/FSU_libsubv1_scholarship_submission_1536242074_55feafcc, 2018.

Ballarotta, M., Ubelmann, C., Pujol, M.-I., Taburet, G., Fournier, F., Legeais, J.-F., Faugère, Y., Delepoulle, A., Chelton, D., Dibarboure, G.,
     et al.: On the resolutions of ocean altimetry maps, Ocean Science, 15, 1091–1109, https://doi.org/10.5194/os-15-1091-2019, 2019.

Bell Jr, T.: Topographically generated internal waves in the open ocean, Journal of Geophysical Research, 80, 320–327,
875   https://doi.org/10.1029/JC080i003p00320, 1975.

Buijsman, M. C., Klymak, J. M., Legg, S., Alford, M. H., Farmer, D., MacKinnon, J. A., Nash, J. D., Park, J.-H., Pickering, A., and
     Simmons, H.: Three-dimensional double-ridge internal tide resonance in Luzon Strait, Journal of Physical Oceanography, 44, 850–869,
     https://doi.org/10.1175/JPO-D-13-024.1, 2014.

Buijsman, M. C., Arbic, B. K., Richman, J. G., Shriver, J. F., Wallcraft, A. J., and Zamudio, L.: Semidiurnal internal tide incoherence in the
880   equatorial p acific, Journal of Geophysical Research: Oceans, 122, 5286–5305, https://doi.org/10.1002/2016JC012590, 2017.

Buijsman, M. C., Stephenson, G. R., Ansong, J. K., Arbic, B. K., Green, J. M., Richman, J. G., Shriver, J. F., Vic, C., Wallcraft, A. J., and
     Zhao, Z.: On the interplay between horizontal resolution and wave drag and their effect on tidal baroclinic mode waves in realistic global
     ocean simulations, Ocean Modelling, 152, 101 656, https://doi.org/10.1016/j.ocemod.2020.101656, 2020.

Callies, J., Ferrari, R., Klymak, J. M., and Gula, J.: Seasonality in submesoscale turbulence, Nature communications, 6, 6862,
885   https://doi.org/10.1038/ncomms7862, 2015.

Carrere, L., Arbic, B. K., Dushaw, B., Egbert, G., Erofeeva, S., Lyard, F., Ray, R. D., Ubelmann, C., Zaron, E., Zhao, Z., et al.: Accuracy
     assessment of global internal-tide models using satellite altimetry, Ocean Science, 17, 147–180, https://doi.org/10.5194/os-17-147-2021,
     2021.

Carter, G. S., Merrifield, M., Becker, J. M., Katsumata, K., Gregg, M., Luther, D., Levine, M., Boyd, T. J., and Firing, Y.: Ener-
890   getics of M 2 barotropic-to-baroclinic tidal conversion at the Hawaiian Islands, Journal of Physical Oceanography, 38, 2205–2223,
     https://doi.org/10.1175/2008JPO3860.1, 2008.

Couvelard, X.: Structure et dynamique des jets barotropes créés pas les îles du Pacifique Sud-Ouest., Ph.D. thesis, Université Paul Sabatier-
     Toulouse III, 2007.

Couvelard, X., Marchesiello, P., Gourdeau, L., and Lefèvre, J.: Barotropic zonal jets induced by islands in the southwest Pacific, Journal of
895   Physical Oceanography, 38, 2185–2204, https://doi.org/10.1175/2008JPO3903.1, 2008.

Cravatte, S., Kestenare, E., Eldin, G., Ganachaud, A., Lefèvre, J., Marin, F., Menkes, C., and Aucan, J.: Regional circulation around New
     Caledonia from two decades of observations, Journal of Marine Systems, 148, 249–271, https://doi.org/10.1016/j.jmarsys.2015.03.004,
     2015.

de Lavergne, C., Falahat, S., Madec, G., Roquet, F., Nycander, J., and Vic, C.: Toward global maps of internal tide energy sinks, Ocean Modelling, 137, 52–75, https://doi.org/10.1016/j.ocemod.2019.03.010, 2019.

de Lavergne, C., Vic, C., Madec, G., Roquet, F., Waterhouse, A. F., Whalen, C., Cuypers, Y., Bouruet-Aubertot, P., Ferron, B., and Hibiya, T.: A parameterization of local and remote tidal mixing, Journal of Advances in Modeling Earth Systems, 12, e2020MS002 065, https://doi.org/10.1029/2020MS002065, 2020.

Debreu, L., Vouland, C., and Blayo, E.: AGRIF: Adaptive grid refinement in Fortran, Computers & Geosciences, 34, 8–13, https://doi.org/10.1016/j.cageo.2007.01.009, 2008.

Derville, S., Torres, L. G., Zerbini, A. N., Oremus, M., and Garrigue, C.: Horizontal and vertical movements of humpback whales inform the use of critical pelagic habitats in the western South Pacific, Scientific Reports, 10, 4871, https://doi.org/10.1038/s41598-020-61771-z, 2020.

Dufau, C., Orsztynowicz, M., Dibarboure, G., Morrow, R., and Le Traon, P.-Y.: Mesoscale resolution capability of altimetry: Present and future, Journal of Geophysical Research: Oceans, 121, 4910–4927, https://doi.org/10.1002/2015JC010904, 2016.

Dunphy, M. and Lamb, K. G.: Focusing and vertical mode scattering of the first mode internal tide by mesoscale eddy interaction, Journal of Geophysical Research: Oceans, 119, 523–536, https://doi.org/10.1002/2013JC009293, 2014.

Dunphy, M., Ponte, A. L., Klein, P., and Le Gentil, S.: Low-mode internal tide propagation in a turbulent eddy field, Journal of Physical Oceanography, 47, 649–665, https://doi.org/10.1175/JPO-D-16-0099.1, 2017.

Durand, F., Marin, F., Fuda, J.-L., and Terre, T.: The east caledonian current: a case example for the intercomparison between altika and in situ measurements in a boundary current, Marine Geodesy, 40, 1–22, https://doi.org/10.1080/01490419.2016.1258375, 2017.

Dushaw, B.: An empirical model for mode-1 internal tides derived from satellite altimetry: Computing accurate tidal predictions at arbitrary points over the world oceans, University of Washington Applied Physics Laboratory Tech. Rep, 2015.

Dushaw, B. D., Howe, B. M., Cornuelle, B. D., Worcester, P. F., and Luther, D. S.: Barotropic and baroclinic tides in the central North Pacific Ocean determined from long-range reciprocal acoustic transmissions, Journal of Physical Oceanography, 25, 631–647, https://doi.org/10.1175/1520-0485(1995)025<0631:BABTIT>2.0.CO;2, 1995.

d'Ovidio, F., Pascual, A., Wang, J., Doglioli, A. M., Jing, Z., Moreau, S., Grégori, G., Swart, S., Speich, S., Cyr, F., et al.: Frontiers in fine-scale in situ studies: Opportunities during the swot fast sampling phase, Frontiers in Marine Science, 6, 168, https://doi.org/10.3389/fmars.2019.00168, 2019.

Egbert, G. D. and Ray, R. D.: Estimates of M2 tidal energy dissipation from TOPEX/Poseidon altimeter data, Journal of Geophysical Research: Oceans, 106, 22 475–22 502, https://doi.org/10.1029/2000JC000699, 2001.

Falahat, S., Nycander, J., Roquet, F., and Zarroug, M.: Global calculation of tidal energy conversion into vertical normal modes, Journal of Physical Oceanography, 44, 3225–3244, https://doi.org/10.1175/JPO-D-14-0002.1, 2014.

Fu, L.-L. and Ferrari, R.: Observing Oceanic Submesoscale Processes From Space, Eos, Transactions American Geophysical Union, 89, 488–488, https://doi.org/10.1029/2008EO480003, _eprint: https://onlinelibrary.wiley.com/doi/pdf/10.1029/2008EO480003, 2008.

Fu, L.-L. and Ubelmann, C.: On the transition from profile altimeter to swath altimeter for observing global ocean surface topography, Journal of Atmospheric and Oceanic Technology, 31, 560–568, https://doi.org/10.1175/JTECH-D-13-00109.1, 2014.

Fu, L.-L., Alsdorf, D., Morrow, R., Rodriguez, E., and Mognard, N.: SWOT: the Surface Water and Ocean Topography Mission: wide-swath altimetric elevation on Earth, Tech. rep., Pasadena, CA: Jet Propulsion Laboratory, National Aeronautics and Space . . . , http://hdl.handle.net/2014/41996, 2012.

Ganachaud, A., Vega, A., Rodier, M., Dupouy, C., Maes, C., Marchesiello, P., Eldin, G., Ridgway, K., and Le Borgne, R.: Observed impact of upwelling events on water properties and biological activity off the southwest coast of New Caledonia, Marine Pollution Bulletin, 61, 449–464, https://doi.org/10.1016/j.marpolbul.2010.06.042, 2010.

Gardes, L., Tessier, E., Allain, V., Alloncle, N., Baudat-Franceschi, J., Butaud, J., Collot, J., Etaix-Bonnin, R., Hubert, A., Jourdan, H., et al.: Analyse stratégique de l'Espace maritime de la Nouvelle-Calédonie–vers une gestion intégrée, Nouméa: Agence des aires marines protégées, https://doi.org/10.13140/RG.2.1.2888.0803, 2014.

Garrett, C. and Kunze, E.: Internal tide generation in the deep ocean, Annu. Rev. Fluid Mech., 39, 57–87, https://doi.org/10.1146/annurev.fluid.39.050905.110227, 2007.

Gaspar, P., Grégoris, Y., and Lefevre, J.-M.: A simple eddy kinetic energy model for simulations of the oceanic vertical mixing: Tests at station Papa and Long-Term Upper Ocean Study site, Journal of Geophysical Research: Oceans, 95, 16 179–16 193, https://doi.org/10.1029/JC095iC09p16179, 1990.

Guo, Z., Wang, S., Cao, A., Xie, J., Song, J., and Guo, X.: Refraction of the M2 internal tides by mesoscale eddies in the South China Sea, Deep Sea Research Part I: Oceanographic Research Papers, 192, 103 946, https://doi.org/10.1016/j.dsr.2022.103946, 2023.

Hendershott, M. C.: Long waves and ocean tides, Evolution of physical oceanography, 1981.

Hersbach, H., Bell, B., Berrisford, P., Hirahara, S., Horányi, A., Muñoz-Sabater, J., Nicolas, J., Peubey, C., Radu, R., Schepers, D., et al.: The ERA5 global reanalysis, Quarterly Journal of the Royal Meteorological Society, 146, 1999–2049, https://doi.org/10.1002/qj.3803, 2020.

Jan, S. and Chen, C.-T. A.: Potential biogeochemical effects from vigorous internal tides generated in Luzon Strait: a case study at the southernmost coast of Taiwan, Journal of Geophysical Research: Oceans, 114, https://doi.org/10.1029/2008JC004887, 2009.

Jayne, S. R. and St. Laurent, L. C.: Parameterizing tidal dissipation over rough topography, Geophysical Research Letters, 28, 811–814, https://doi.org/10.1029/2000GL012044, 2001.

Jeon, C.-H., Buijsman, M. C., Wallcraft, A. J., Shriver, J. F., Arbic, B. K., Richman, J. G., and Hogan, P. J.: Improving surface tidal accuracy through two-way nesting in a global ocean model, Ocean Modelling, 137, 98–113, https://doi.org/10.1016/j.ocemod.2019.03.007, 2019.

Kelly, S., Nash, J., and Kunze, E.: Internal-tide energy over topography, Journal of Geophysical Research: Oceans, 115, https://doi.org/10.1029/2009JC005618, 2010.

Kelly, S., Jones, N., Nash, J., and Waterhouse, A.: The geography of semidiurnal mode-1 internal-tide energy loss, Geophysical Research Letters, 40, 4689–4693, https://doi.org/10.1002/grl.50872, 2013.

Kelly, S. M.: The vertical mode decomposition of surface and internal tides in the presence of a free surface and arbitrary topography, Journal of Physical Oceanography, 46, 3777–3788, https://doi.org/10.1175/JPO-D-16-0131.1, 2016.

Kelly, S. M. and Lermusiaux, P. F.: Internal-tide interactions with the Gulf Stream and Middle Atlantic Bight shelfbreak front, Journal of Geophysical Research: Oceans, 121, 6271–6294, https://doi.org/10.1002/2016JC011639, 2016.

Keppler, L., Cravatte, S., Chaigneau, A., Pegliasco, C., Gourdeau, L., and Singh, A.: Observed characteristics and vertical structure of mesoscale eddies in the southwest tropical Pacific, Journal of Geophysical Research: Oceans, 123, 2731–2756, https://doi.org/10.1002/2017JC013712, 2018.

Kerry, C. G., Powell, B. S., and Carter, G. S.: Effects of remote generation sites on model estimates of M2 internal tides in the Philippine Sea, Journal of Physical Oceanography, 43, 187–204, https://doi.org/10.1175/JPO-D-12-081.1, 2013.

Kerry, C. G., Powell, B. S., and Carter, G. S.: The impact of subtidal circulation on internal tide generation and propagation in the Philippine Sea, Journal of Physical Oceanography, 44, 1386–1405, https://doi.org/10.1175/JPO-D-13-0142.1, 2014.

Kerry, C. G., Powell, B. S., and Carter, G. S.: Quantifying the incoherent M 2 internal tide in the Philippine Sea, Journal of Physical Oceanography, 46, 2483–2491, https://doi.org/10.1175/JPO-D-16-0023.1, 2016.

975 Kessler, W. S. and Cravatte, S.: Mean circulation of the Coral Sea, Journal of Geophysical Research: Oceans, 118, 6385–6410, https://doi.org/10.1002/2013JC009117, 2013.

Kunze, E.: Internal-wave-driven mixing: Global geography and budgets, Journal of Physical Oceanography, 47, 1325–1345, https://doi.org/10.1175/JPO-D-16-0141.1, 2017a.

Kunze, E.: The internal-wave-driven meridional overturning circulation, Journal of Physical Oceanography, 47, 2673–2689, 980 https://doi.org/10.1175/JPO-D-16-0141.1, 2017b.

Lahaye, N., Gula, J., and Roullet, G.: Sea Surface Signature of Internal Tides, Geophysical Research Letters, 46, 3880–3890, https://doi.org/10.1029/2018GL081848, 2019.

Lahaye, N., Gula, J., and Roullet, G.: Internal Tide Cycle and Topographic Scattering Over the North Mid-Atlantic Ridge, Journal of Geophysical Research: Oceans, 125, https://doi.org/10.1029/2020JC016376, 2020.

985 Laurent, L. C. S. and Nash, J. D.: An examination of the radiative and dissipative properties of deep ocean internal tides, Deep Sea Research Part II: Topical Studies in Oceanography, 51, 3029–3042, https://doi.org/10.1016/j.dsr2.2004.09.008, 2004.

Laurent, L. S., Stringer, S., Garrett, C., and Perrault-Joncas, D.: The generation of internal tides at abrupt topography, Deep Sea Research Part I: Oceanographic Research Papers, 50, 987–1003, https://doi.org/10.1016/S0967-0637(03)00096-7, 2003.

Le Guillou, F., Lahaye, N., Ubelmann, C., Metref, S., Cosme, E., Ponte, A., Le Sommer, J., Blayo, E., and Vidard, A.: Joint Estima-990 tion of Balanced Motions and Internal Tides From Future Wide-Swath Altimetry, Journal of Advances in Modeling Earth Systems, 13, e2021MS002 613, https://doi.org/10.1029/2021MS002613, _eprint: https://onlinelibrary.wiley.com/doi/pdf/10.1029/2021MS002613, 2021.

Le Traon, P.-Y., Klein, P., Hua, B. L., and Dibarboure, G.: Do altimeter wavenumber spectra agree with the interior or surface quasigeostrophic theory?, Journal of Physical Oceanography, 38, 1137–1142, https://doi.org/10.1175/2007JPO3806.1, 2008.

995 Lefauve, A., Muller, C., and Melet, A.: A three-dimensional map of tidal dissipation over abyssal hills, Journal of Geophysical Research: Oceans, 120, 4760–4777, https://doi.org/10.1002/2014JC010598, 2015.

Legg, S. and Huijts, K. M.: Preliminary simulations of internal waves and mixing generated by finite amplitude tidal flow over isolated topography, Deep Sea Research Part II: Topical Studies in Oceanography, 53, 140–156, https://doi.org/10.1016/j.dsr2.2005.09.014, 2006.

Leichter, J. J., Stewart, H. L., and Miller, S. L.: Episodic nutrient transport to Florida coral reefs, Limnology and Oceanography, 48, 1394–1000 1407, https://doi.org/10.4319/lo.2003.48.4.1394, 2003.

Lyard, F. H., Allain, D. J., Cancet, M., Carrère, L., and Picot, N.: FES2014 global ocean tide atlas: design and performance, Ocean Science, 17, 615–649, https://doi.org/10.5194/os-17-615-2021, 2021.

MacKinnon, J. A., Zhao, Z., Whalen, C. B., Waterhouse, A. F., Trossman, D. S., Sun, O. M., Laurent, L. C. S., Simmons, H. L., Polzin, K., Pinkel, R., et al.: Climate process team on internal wave–driven ocean mixing, Bulletin of the American Meteorological Society, 98, 1005 2429–2454, https://doi.org/10.1175/BAMS-D-16-0030.1, 2017.

Madec, G. and Team, N. S.: NEMO ocean engine, no. 27 in Scientific Notes of Climate Modelling Center, Zenodo, https://doi.org/10.5281/zenodo.1464816, backup Publisher: Institut Pierre-Simon Laplace (IPSL) ISSN: 1288-1619.

Magalhães, J. M., Da Silva, J., Buijsman, M. C., and Garcia, C.: Effect of the North Equatorial Counter Current on the generation and propagation of internal solitary waves off the Amazon shelf (SAR observations), Ocean Science, 12, 243–255, https://doi.org/10.5194/os-1010 12-243-2016, 2016.

Mazloff, M. R., Cornuelle, B., Gille, S. T., and Wang, J.: The Importance of Remote Forcing for Regional Modeling of Internal Waves, Journal of Geophysical Research: Oceans, 125, https://doi.org/10.1029/2019JC015623, 2020.

McDougall, T. J. and Barker, P. M.: Getting started with TEOS-10 and the Gibbs Seawater (GSW) oceanographic toolbox, Scor/Iapso WG, 127, 1–28, 2011.

1015 Melet, A., Hallberg, R., Legg, S., and Polzin, K.: Sensitivity of the ocean state to the vertical distribution of internal-tide-driven mixing, Journal of Physical Oceanography, 43, 602–615, https://doi.org/10.1175/JPO-D-12-055.1, 2013.

Menkès, C. E., Allain, V., Rodier, M., Gallois, F., Lebourges-Dhaussy, A., Hunt, B. P., Smeti, H., Pagano, M., Josse, E., Daroux, A., et al.: Seasonal oceanography from physics to micronekton in the south-west Pacific, Deep Sea Research Part II: Topical Studies in Oceanography, 113, 125–144, https://doi.org/10.1016/j.dsr2.2014.10.026, 2015.

1020 Merrifield, M. A. and Holloway, P. E.: Model estimates of M2 internal tide energetics at the Hawaiian Ridge, Journal of Geophysical Research: Oceans, 107, 5–1, https://doi.org/10.1029/2001JC000996, 2002.

Messié, M., Petrenko, A., Doglioli, A. M., Martinez, E., and Alvain, S.: Basin-scale biogeochemical and ecological impacts of islands in the tropical Pacific Ocean, Nature Geoscience, 15, 469–474, https://doi.org/10.1038/s41561-022-00957-8, 2022.

Morrow, R., Fu, L.-L., Ardhuin, F., Benkiran, M., Chapron, B., Cosme, E., d'Ovidio, F., Farrar, J. T., Gille, S. T., Lapeyre, G., et al.: Global
1025 observations of fine-scale ocean surface topography with the Surface Water and Ocean Topography (SWOT) mission, Frontiers in Marine Science, 6, 232, https://doi.org/10.3389/fmars.2019.00232, 2019.

Muacho, S., Da Silva, J., Brotas, V., and Oliveira, P.: Effect of internal waves on near-surface chlorophyll concentration and primary production in the Nazaré Canyon (west of the Iberian Peninsula), Deep Sea Research Part I: Oceanographic Research Papers, 81, 89–96, https://doi.org/10.1016/j.dsr.2013.07.012, 2013.

1030 Munk, W. and Wunsch, C.: Abyssal recipes II: Energetics of tidal and wind mixing, Deep Sea Research Part I: Oceanographic Research Papers, 45, 1977–2010, https://doi.org/10.1016/S0967-0637(98)00070-3, 1998.

Nash, J. D., Kelly, S. M., Shroyer, E. L., Moum, J. N., and Duda, T. F.: The unpredictable nature of internal tides on continental shelves, Journal of Physical Oceanography, 42, 1981–2000, https://doi.org/10.1175/JPO-D-12-028.1, 2012.

Nelson, A. D., Arbic, B. K., Zaron, E. D., Savage, A. C., Richman, J. G., Buijsman, M. C., and Shriver, J. F.: Toward Realistic Non-
1035 stationarity of Semidiurnal Baroclinic Tides in a Hydrodynamic Model, Journal of Geophysical Research: Oceans, 124, 6632–6642, https://doi.org/10.1029/2018JC014737, 2019.

Nikurashin, M. and Legg, S.: A mechanism for local dissipation of internal tides generated at rough topography, Journal of Physical Oceanography, 41, 378–395, https://doi.org/10.1175/2010JPO4522.1, 2011.

Niwa, Y. and Hibiya, T.: Numerical study of the spatial distribution of the M2 internal tide in the Pacific Ocean, Journal of Geophysical
1040 Research: Oceans, 106, 22 441–22 449, https://doi.org/10.1029/2000JC000770, 2001.

Niwa, Y. and Hibiya, T.: Three-dimensional numerical simulation of M2 internal tides in the East China Sea, Journal of Geophysical Research: Oceans, 109, https://doi.org/10.1029/2003JC001923, 2004.

Nugroho, D.: The tides in a general circulation model in the indonesian sras, Ph.D. thesis, Université Paul Sabatier-Toulouse III, 2017.

Nycander, J.: Generation of internal waves in the deep ocean by tides, Journal of Geophysical Research: Oceans, 110,
1045 https://doi.org/10.1029/2004JC002487, 2005.

Olbers, D., Pollmann, F., and Eden, C.: On PSI interactions in internal gravity wave fields and the decay of baroclinic tides, Journal of Physical Oceanography, 50, 751–771, https://doi.org/10.1175/JPO-D-19-0224.1, 2020.

Park, J.-H. and Watts, D. R.: Internal tides in the southwestern Japan/East Sea, Journal of Physical Oceanography, 36, 22–34, https://doi.org/10.1175/JPO2846.1, 2006.

1050 Payri, C.-E. and de Forges, B. R.: Compendium of marine species from New Caledonia, IRD (Institut de recherche pour le développement), 2006.

Payri, C. E., Allain, V., Aucan, J., David, C., David, V., Dutheil, C., Loubersac, L., Menkes, C., Pelletier, B., Pestana, G., et al.: New caledonia, in: World Seas: An Environmental Evaluation, pp. 593–618, Elsevier, https://doi.org/10.1016/B978-0-08-100853-9.00035-X, 2019.

1055 Pelletier, B.: Geology of the New Caledonia region and its implications for the study of the New Caledonian biodiversity, Compendium of marines species from New Caledonia, Dossiers Scientifiques et Techniques, II7, pp. 19–32, 2007.

Ponte, A. L. and Klein, P.: Incoherent signature of internal tides on sea level in idealized numerical simulations, Geophysical Research Letters, 42, 1520–1526, https://doi.org/10.1002/2014GL062583, 2015.

Ponte, A. L., Klein, P., Dunphy, M., and Le Gentil, S.: Low-mode internal tides and balanced dynamics disentanglement in al-
1060 timetric observations: Synergy with surface density observations, Journal of Geophysical Research: Oceans, 122, 2143–2155, https://doi.org/10.1002/2016JC012214, 2017.

Qiu, B. and Chen, S.: Seasonal modulations in the eddy field of the South Pacific Ocean, Journal of Physical Oceanography, 34, 1515–1527, https://doi.org/10.1175/1520-0485(2004)034<1515:SMITEF>2.0.CO;2, 2004.

Qiu, B., Scott, R. B., and Chen, S.: Length scales of eddy generation and nonlinear evolution of the seasonally modulated South Pacific
1065 Subtropical Countercurrent, Journal of Physical Oceanography, 38, 1515–1528, https://doi.org/10.1175/2007JPO3856.1, 2008.

Qiu, B., Chen, S., and Kessler, W. S.: Source of the 70-day mesoscale eddy variability in the Coral Sea and the North Fiji Basin, Journal of Physical Oceanography, 39, 404–420, https://doi.org/10.1175/2008JPO3988.1, 2009.

Qiu, B., Chen, S., Klein, P., Wang, J., Torres, H., Fu, L.-L., and Menemenlis, D.: Seasonality in Transition Scale from Balanced to Unbalanced Motions in the World Ocean, Journal of Physical Oceanography, 48, 591–605, https://doi.org/10.1175/JPO-D-17-0169.1, 2018.

1070 Qu, T. and Lindstrom, E. J.: A climatological interpretation of the circulation in the western South Pacific, Journal of Physical Oceanography, 32, 2492–2508, https://doi.org/10.1175/1520-0485(2002)032<2492:ACIOTC>2.0.CO;2, 2002.

Ray, R. D. and Zaron, E. D.: M2 internal tides and their observed wavenumber spectra from satellite altimetry, Journal of Physical Oceanography, 46, 3–22, https://doi.org/10.1175/JPO-D-15-0065.1, 2016.

Renault, L., Molemaker, M. J., McWilliams, J. C., Shchepetkin, A. F., Lemarié, F., Chelton, D., Illig, S., and Hall, A.: Modulation of wind
1075 work by oceanic current interaction with the atmosphere, Journal of Physical Oceanography, 46, 1685–1704, https://doi.org/10.1175/JPO-D-15-0232.1, 2016.

Ridgway, K. and Dunn, J.: Mesoscale structure of the mean East Australian Current System and its relationship with topography, Progress in oceanography, 56, 189–222, https://doi.org/10.1016/S0079-6611(03)00004-1, 2003.

Ridgway, K., Dunn, J., and Wilkin, J.: Ocean interpolation by four-dimensional weighted least squares—Application to
1080 the waters around Australasia, Journal of atmospheric and oceanic technology, 19, 1357–1375, https://doi.org/10.1175/1520-0426(2002)019<1357:OIBFDW>2.0.CO;2, 2002.

Rocha, C. B., Gille, S. T., Chereskin, T. K., and Menemenlis, D.: Seasonality of submesoscale dynamics in the Kuroshio Extension, Geophysical Research Letters, 43, 11–304, https://doi.org/10.1002/2016GL071349, 2016.

Roger, J., Pelletier, B., Duphil, M., Lefèvre, J., Aucan, J., Lebellegard, P., Thomas, B., Bachelier, C., and Varillon, D.: The Mw 7.5 Tadine
1085 (Maré, Loyalty Is.) earthquake and related tsunami of December 5, 2018: implications for tsunami hazard assessment in New Caledonia.,

Natural Hazards and Earth System Sciences, Discussions, https://doi. org/10.5194/nhess-2021-58, https://doi.org/10.5194/nhess-2021-58, 2021.

Samadi, S., Bottan, L., Macpherson, E., De Forges, B. R., and Boisselier, M.-C.: Seamount endemism questioned by the geographic distribution and population genetic structure of marine invertebrates, Marine Biology, 149, 1463–1475, https://doi.org/10.1007/s00227-006-0306-4, 2006.

Savage, A. C., Arbic, B. K., Alford, M. H., Ansong, J. K., Farrar, J. T., Menemenlis, D., O'Rourke, A. K., Richman, J. G., Shriver, J. F., Voet, G., Wallcraft, A. J., and Zamudio, L.: Spectral decomposition of internal gravity wave sea surface height in global models, Journal of Geophysical Research: Oceans, 122, 7803–7821, https://doi.org/10.1002/2017JC013009, 2017.

Sérazin, G., Marin, F., Gourdeau, L., Cravatte, S., Morrow, R., and Dabat, M.-L.: Scale-dependent analysis of in situ observations in the mesoscale to submesoscale range around New Caledonia, Ocean Science, 16, 907–925, https://doi.org/10.5194/os-16-907-2020, 2020.

Simmons, H. L., Hallberg, R. W., and Arbic, B. K.: Internal wave generation in a global baroclinic tide model, Deep Sea Research Part II: Topical Studies in Oceanography, 51, 3043–3068, https://doi.org/10.1016/j.dsr2.2004.09.015, 2004.

Smith, S. G. L. and Young, W.: Conversion of the barotropic tide, Journal of Physical Oceanography, 32, 1554–1566, https://doi.org/10.1175/1520-0485(2002)032<1554:COTBT>2.0.CO;2, 2002.

Smith, W. H. and Sandwell, D. T.: Global sea floor topography from satellite altimetry and ship depth soundings, Science, 277, 1956–1962, https://doi.org/10.1126/science.277.5334.1956, 1997.

Soufflet, Y., Marchesiello, P., Lemarié, F., Jouanno, J., Capet, X., Debreu, L., and Benshila, R.: On effective resolution in ocean models, Ocean Modelling, 98, 36–50, https://doi.org/10.1016/j.ocemod.2015.12.004, 2016.

St. Laurent, L. and Garrett, C.: The role of internal tides in mixing the deep ocean, Journal of Physical Oceanography, 32, 2882–2899, https://doi.org/10.1175/1520-0485(2002)032<2882:TROITI>2.0.CO;2, 2002.

St. Laurent, L., Simmons, H., and Jayne, S.: Estimating tidally driven mixing in the deep ocean, Geophysical research letters, 29, 21–1, https://doi.org/10.1029/2002GL015633, 2002.

Tchilibou, M., Gourdeau, L., Lyard, F., Morrow, R., Koch Larrouy, A., Allain, D., and Djath, B.: Internal tides in the Solomon Sea in contrasted ENSO conditions, Ocean Science, 16, 615–635, https://doi.org/10.5194/os-16-615-2020, 2020.

Tchilibou, M., Koch-Larrouy, A., Barbot, S., Lyard, F., Morel, Y., Jouanno, J., and Morrow, R.: Internal tides off the Amazon shelf during two contrasted seasons: interactions with background circulation and SSH imprints, Ocean Science, 18, 1591–1618, https://doi.org/10.5194/os-18-1591-2022, 2022.

Thakur, R., Arbic, B. K., Menemenlis, D., Momeni, K., Pan, Y., Peltier, W. R., Skitka, J., Alford, M. H., and Ma, Y.: Impact of vertical mixing parameterizations on internal gravity wave spectra in regional ocean models, Geophysical Research Letters, 49, e2022GL099 614, https://doi.org/10.1029/2022GL099614, 2022.

Thyng, K. M., Greene, C. A., Hetland, R. D., Zimmerle, H. M., and DiMarco, S. F.: True colors of oceanography: Guidelines for effective and accurate colormap selection, Oceanography, 29, 9–13, https://doi.org/10.5670/oceanog.2016.66, 2016.

Torres, H. S., Klein, P., Menemenlis, D., Qiu, B., Su, Z., Wang, J., Chen, S., and Fu, L.-L.: Partitioning ocean motions into balanced motions and internal gravity waves: A modeling study in anticipation of future space missions, Journal of Geophysical Research: Oceans, 123, 8084–8105, https://doi.org/10.1029/2018JC014438, 2018.

Ubelmann, C., Carrere, L., Durand, C., Dibarboure, G., Faugère, Y., Ballarotta, M., Briol, F., and Lyard, F.: Simultaneous estimation of ocean mesoscale and coherent internal tide sea surface height signatures from the global altimetry record, Ocean Science, 18, 469–481, https://doi.org/10.5194/os-18-469-2022, 2022.

van der Velden, E.: CMasher: Scientific colormaps for making accessible, informative and 'cmashing' plots, The Journal of Open Source
1125   Software, 5, 2004, https://doi.org/10.21105/joss.02004, 2020.

Vergara, O., Morrow, R., Pujol, M.-I., Dibarboure, G., and Ubelmann, C.: Global submesoscale diagnosis using alongtrack satellite altimetry,
    EGUsphere, pp. 1–39, https://doi.org/10.5194/egusphere-2022-1073, 2022.

Vic, C., Garabato, A. C. N., Green, J. M., Spingys, C., Forryan, A., Zhao, Z., and Sharples, J.: The lifecycle of semidiurnal internal tides over
    the northern Mid-Atlantic Ridge, Journal of Physical Oceanography, 48, 61–80, https://doi.org/10.1175/JPO-D-17-0121.1, 2018.

1130 Vic, C., Naveira Garabato, A. C., Green, J. M., Waterhouse, A. F., Zhao, Z., Melet, A., de Lavergne, C., Buijsman, M. C., and Stephenson,
    G. R.: Deep-ocean mixing driven by small-scale internal tides, Nature communications, 10, 2099, https://doi.org/10.1038/s41467-019-
    10149-5, 2019.

Wang, H., Grisouard, N., Salehipour, H., Nuz, A., Poon, M., and Ponte, A. L.: A Deep Learning Approach to Extract Internal Tides Scattered
    by Geostrophic Turbulence, Geophysical Research Letters, 49, https://doi.org/10.1029/2022GL099400, 2022.

1135 Wang, Y.-H., Dai, C.-F., and Chen, Y.-Y.: Physical and ecological processes of internal waves on an isolated reef ecosystem in the South
    China Sea, Geophysical Research Letters, 34, https://doi.org/10.1029/2007GL030658, 2007.

Waterhouse, A. F., MacKinnon, J. A., Nash, J. D., Alford, M. H., Kunze, E., Simmons, H. L., Polzin, K. L., Laurent, L. C. S., Sun, O. M.,
    Pinkel, R., et al.: Global patterns of diapycnal mixing from measurements of the turbulent dissipation rate, Journal of Physical Oceanog-
    raphy, 44, 1854–1872, https://doi.org/10.1175/JPO-D-13-0104.1, 2014.

1140 Wolanski, E. and Pickard, G.: Long-term observations of currents on the central Great Barrier Reef continental shelf, Coral Reefs, 4, 47–57,
    1985.

Wolanski, E., Colin, P., Naithani, J., Deleersnijder, E., and Golbuu, Y.: Large amplitude, leaky, island-generated, internal waves around Palau,
    Micronesia, Estuarine, Coastal and Shelf Science, 60, 705–716, https://doi.org/10.1016/j.ecss.2004.03.009, 2004.

Zaron, E. D.: Mapping the nonstationary internal tide with satellite altimetry, Journal of Geophysical Research: Oceans, 122, 539–554,
1145   https://doi.org/10.1002/2016JC012487, 2017.

Zaron, E. D.: Baroclinic tidal sea level from exact-repeat mission altimetry, Journal of Physical Oceanography, 49, 193–210,
    https://doi.org/10.1175/JPO-D-18-0127.1, 2019.

Zaron, E. D. and Egbert, G. D.: Estimating open-ocean barotropic tidal dissipation: The Hawaiian Ridge, Journal of Physical Oceanography,
    36, 1019–1035, https://doi.org/10.1175/JPO2878.1, 2006.

1150 Zhao, Z., Alford, M. H., MacKinnon, J. A., and Pinkel, R.: Long-range propagation of the semidiurnal internal tide from the Hawaiian Ridge,
    Journal of Physical Oceanography, 40, 713–736, https://doi.org/10.1175/2009JPO4207.1, 2010.

Zhao, Z., Alford, M. H., Girton, J. B., Rainville, L., and Simmons, H. L.: Global observations of open-ocean mode-1 M 2 internal tides,
    Journal of Physical Oceanography, 46, 1657–1684, https://doi.org/10.1175/JPO-D-15-0105.1, 2016.

Zilberman, N., Becker, J., Merrifield, M., and Carter, G.: Model estimates of M2 internal tide generation over Mid-Atlantic Ridge topography,
1155   Journal of Physical Oceanography, 39, 2635–2651, https://doi.org/10.1175/2008JPO4136.1, 2009.

Zilberman, N., Merrifield, M., Carter, G., Luther, D., Levine, M., and Boyd, T. J.: Incoherent nature of M 2 internal tides at the Hawaiian
    Ridge, Journal of physical oceanography, 41, 2021–2036, https://doi.org/10.1175/JPO-D-10-05009.1, 2011.

Table 1. Full-domain, area-integrated barotropic-to-baroclinic conversion in GW for each tidal constituent (M2, S2, N2, K1, O1) with their respective contribution to the total in %.

	Total	M2	S2	N2	K1	O1
Conversion [GW]	19.03 (100 %)	15.27 (80.2 %)	2.04 (10.7 %)	0.92 (4.8 %)	0.64 (3.4 %)	0.16 (0.8 %)
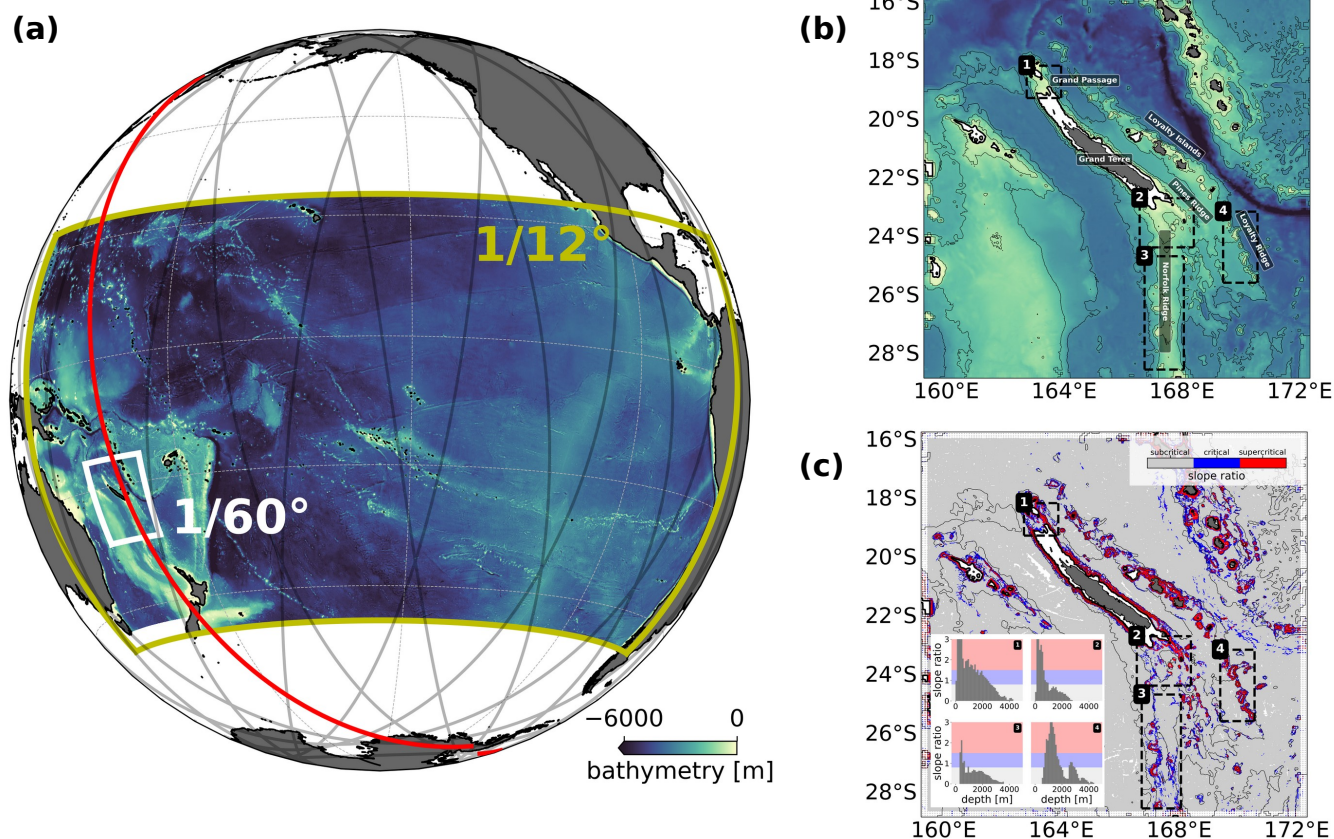
Figure 1. (a) Model set-up showing the host grid domain (TROPICO12, yellow box) and the nesting grid (CALEDO60, white box) including the bathymetry (shading), and the SWOT CalVal orbit (black transparent lines) with the highlighted ground track (red line) that crosses the CALEDO60 domain. CALEDO60 (b) bathymetry and (c) M2 tide slope ratio α between topographic slope and wave slope s, divided into subcritical (gray, $\alpha < 0.8$ s), critical (blue, 0.8 s $< \alpha < 1.5$ s), and supercritical (red, $\alpha > 1.5$ s) slopes. Note that white shaded grid points are associated with zero bathymetry gradient. The hatched contour indicates the shallow waters of the New Caledonian lagoon enclosed by the barrier reef. The thin black lines represent the 1000 m, 2000 m, and 3000 m depth contours. The thick black line is the 100 m depth contour representative for the New Caledonian lagoon. The numbered, black boxes represent the hotspots of internal tide generation (1: North, 2: South, 3: Norfolk Ridge, 4: Loyalty Ridge) for which the distribution of slope ratio as a function of depth is given in the inset of (b).
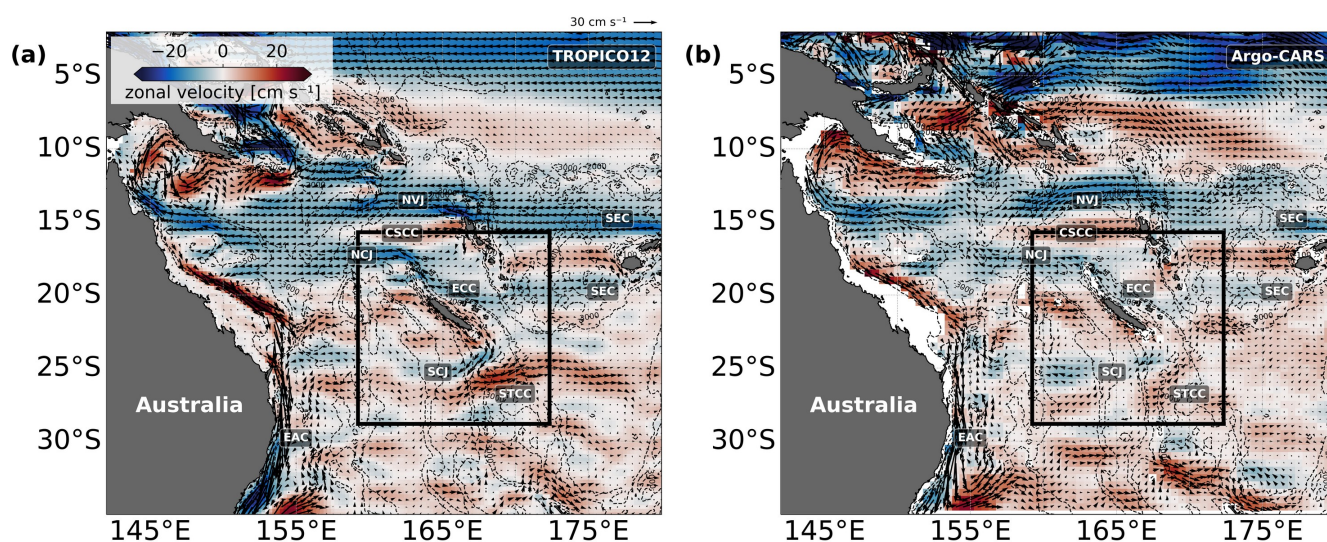
Figure 2. Coral Sea near-surface (20-100 m) regional circulation illustrating zonal velocity (shading) and velocity vectors from (a) TROPICO12 (2014-2018 mean) and (b) Argo-CARS merged velocity product (Kessler and Cravatte, 2013). The black box indicates the CALEDO60 domain. The major currents are labeled: South Equatorial Current (SEC), North Vanuatu Jet (NVJ), Coral Sea Counter Current (CSCC), North Caledonian Jet (NCJ), East Caledonian Current (ECC), South Caledonian Jet (SCJ), South Tropical Counter Current (STCC), and East Australian Current (EAC).
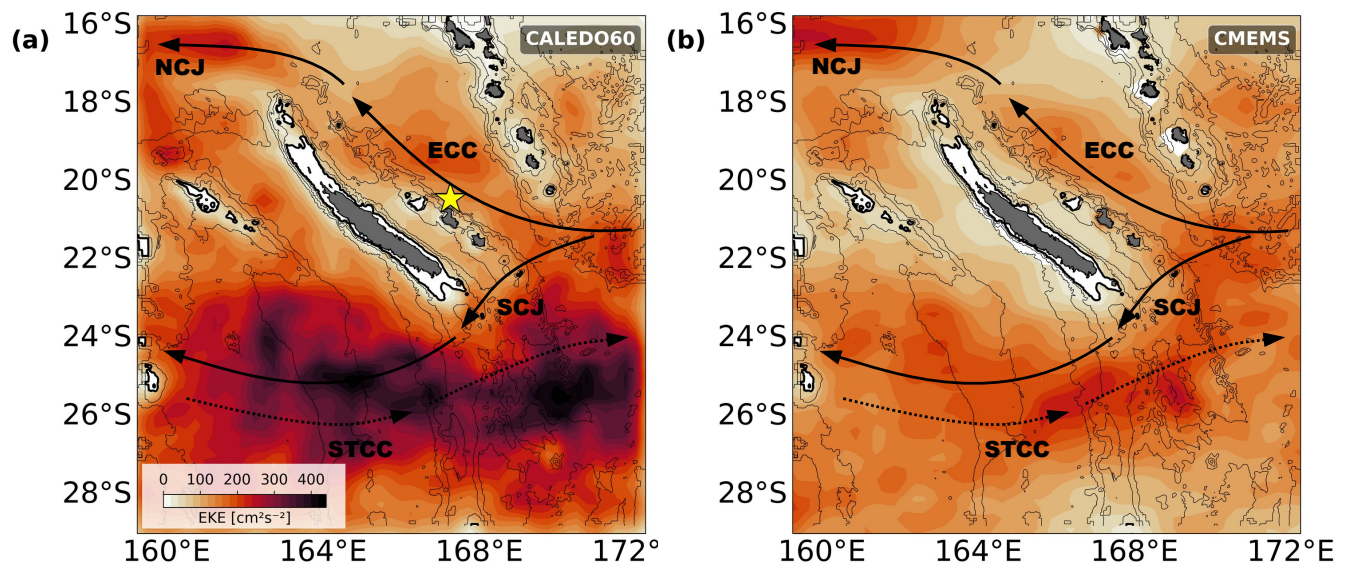
Figure 3. Mesoscale EKE derived from SSH for (a) CALEDO60 and (b) CMEMS altimeter products and averaged for the period 2014-2018. Currents are labeled as in Fig. 2. The location of the in-situ mooring (cf Sect. 2.3.3) is indicated by the yellow star.
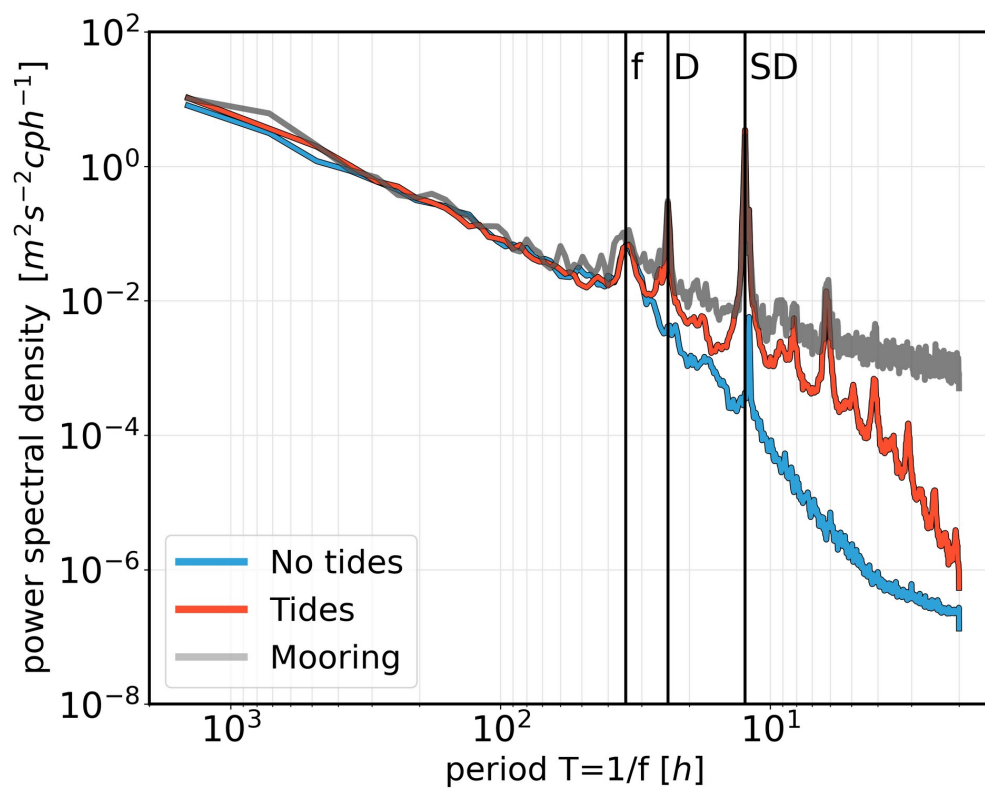
Figure 4. Power spectral density of near surface (20-100 m) horizontal kinetic energy for CALEDO60 with (blue) and without (orange) tidal forcing for the full model time series near 167.25° E, 20.43° S in the New Caledonian eastern boundary current (see Fig. 3a). The energy spectra are compared to a mooring time series that was deployed between November 2010 and October 2011 (Durand et al., 2017). The vertical black lines indicate the inertial (f), diurnal (D), and semidiurnal SD period.
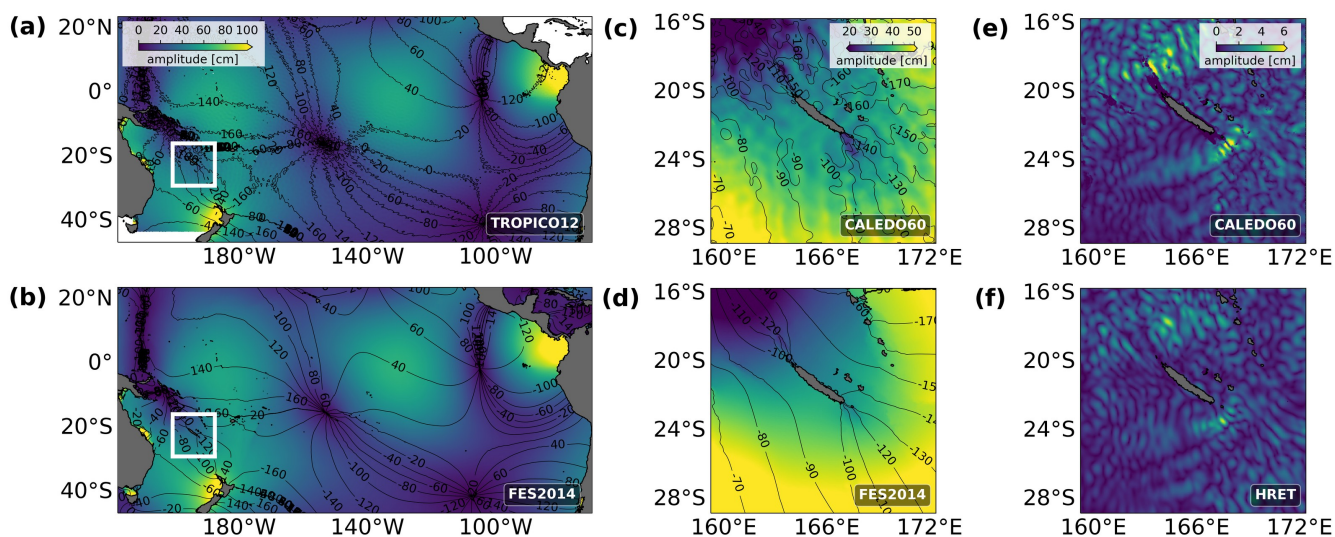
Figure 5. Barotropic M2 SSH amplitude (shading) and phase (contour) for (a) TROPICO12 and (c) CALEDO60 based on a 1-year (2014) harmonic analysis (assuming that the model SSH is dominated by the barotropic tide) and in comparison to the global tide atlas FES2014 for (b) TROPICO12 and (d) CALEDO60. (e) Total baroclinic M2 SSH amplitude for CALEDO60 derived from a vertical mode decomposition compared to the empirical estimates of the High Resolution Empirical Tide (HRET) model. The inset in (a) and (b) indicates the location of the CALEDO60 domain.
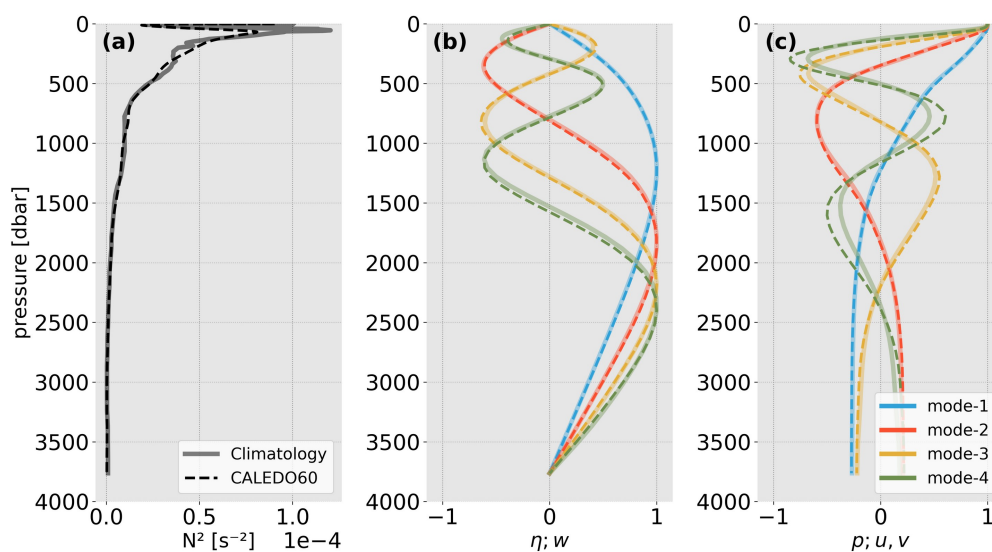
Figure 6. (a) Buoyancy frequency (N^2) for a representative profile at $166°$ E, $26°$ S from the CARS2009 climatology (solid) and CALEDO60 (dashed). Normalized baroclinic modal structures for (b) displacement η and vertical velocity w, and (c) pressure p and horizontal velocity u, v for the four lowest modes are also shown.
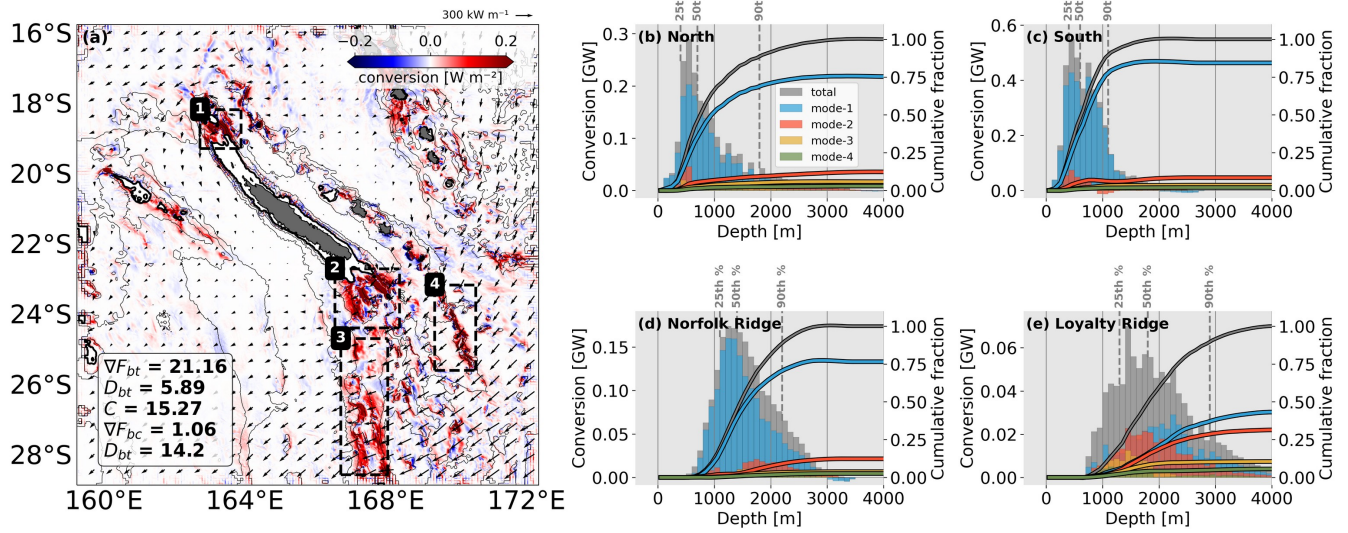
Figure 7. (a) M2 barotropic-to-baroclinic conversion including barotropic energy flux vectors and the full-domain area-integral of the barotropic energy flux divergence (∇F_{bt}), barotropic energy dissipation (D_{bt}), barotropic-to-baroclinic conversion (C), baroclinic energy flux divergence (∇F_{bc}), and baroclinic energy dissipation (D_{bc}) in GW. Histograms of the regional area-integrated conversion (total baroclinic and four lowest modes) as a function of generation depth divided into 100 m depth bins for (b) North, (c) South, (d) Norfolk Ridge, and (e) Loyalty Ridge. The 25th, 50th, and 90th percentile as well as the normalized cumulative fraction are also shown.
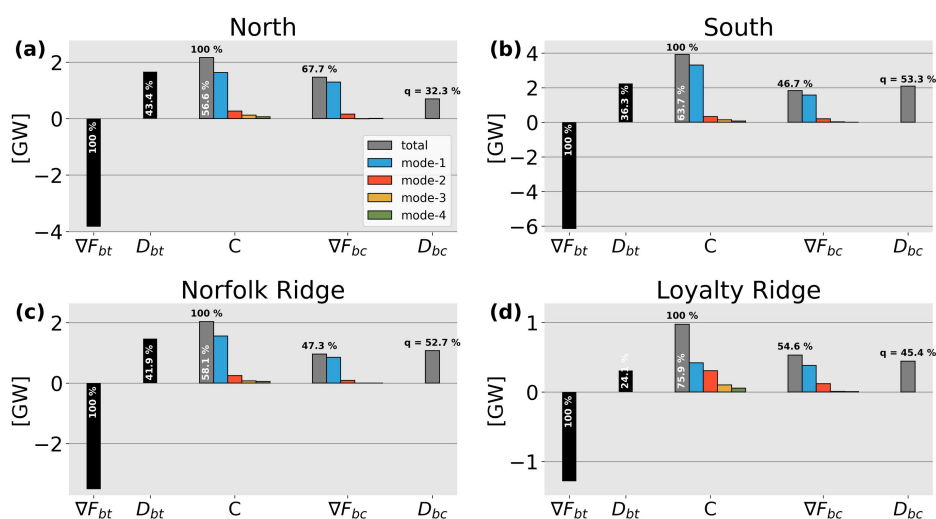
Figure 8. Bar plots of the regional M2 energy budgets for (a) North, (b) South, (c) Norfolk Ridge, (d) Loyalty Ridge including the barotropic energy flux divergence (∇F_{bt}), barotropic energy dissipation (D_{bt}), conversion (C), baroclinic energy flux divergence (∇F_{bc}), and baroclinic energy dissipation (D_{bc}) for the total baroclinic and the four lowest modes. The white labeled percentage values refer to the energy budget of barotropic energy budget whereas the black labeled percentage values are associated with the total baroclinic energy budget relative to the conversion term. The fraction of locally dissipated energy is given by q.
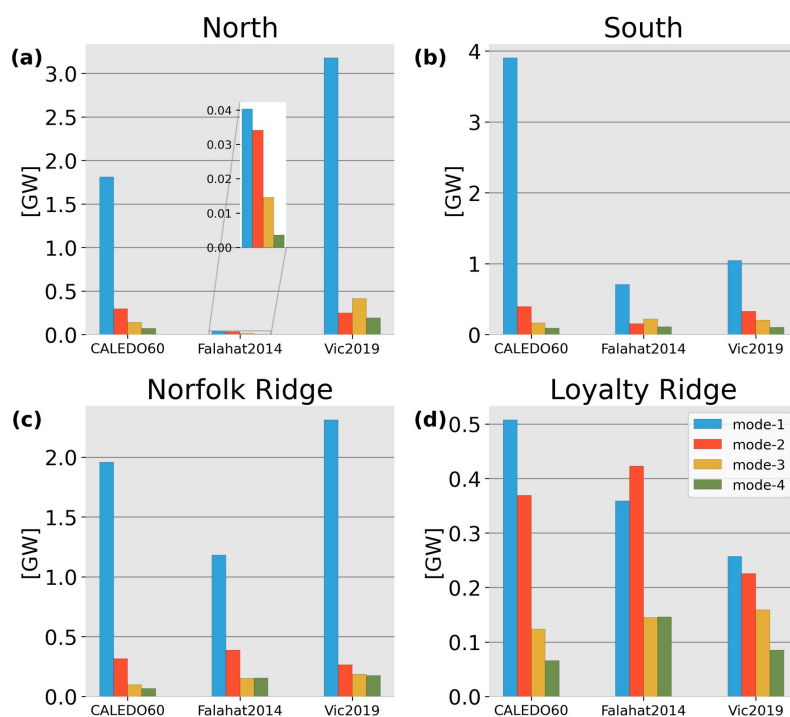
Figure 9. M2 barotropic-to-baroclinic energy conversion in GW for the four lowest modes in comparison with the semi-analytical estimates from Falahat et al. (2014) and Vic et al. (2019) integrated over (a) *North*, (b) *South*, (c), *Norfolk Ridge*, and (d) *Loyalty Ridge*.
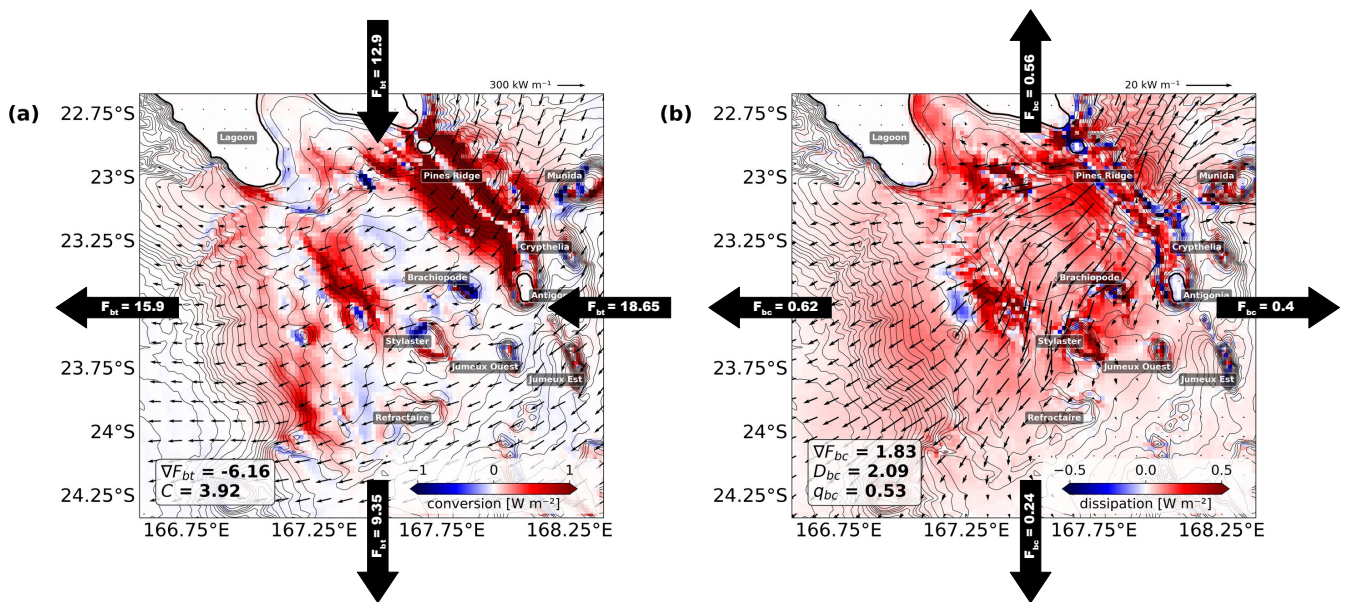
Figure 10. Regional M2 energy budget exemplary shown for the *South* (2) domain with (a) the M2 barotropic-to-baroclinic conversion (shading) overlaid by the M2 barotropic energy flux (vectors) and (b) the depth-integrated M2 baroclinic energy dissipation overlaid by the depth-integrated M2 baroclinic energy flux (vectors). The area-integrated values for the barotropic energy flux divergence (∇F_{bt}) and barotropic-to-baroclinic conversion C in (a) and the baroclinic energy flux divergence (∇F_{bc}), the baroclinic energy dissipation D_{bc}, as well as the ratio of locally dissipated baroclinic energy q_{bc} in (b) are also given. The incoming/outgoing (a) barotropic and (b) baroclinic energy flux with integrated values along the boundary are illustrated at the lateral boundaries of the domain indicating the net direction of energy propagation. All integrated quantities are given in GW. The Pines Ridge, the lagoon and the most prominent seamounts are labeled. The depth contour interval is 100 m where the thick black line is the 100 m depth contour representative for the New Caledonian lagoon.
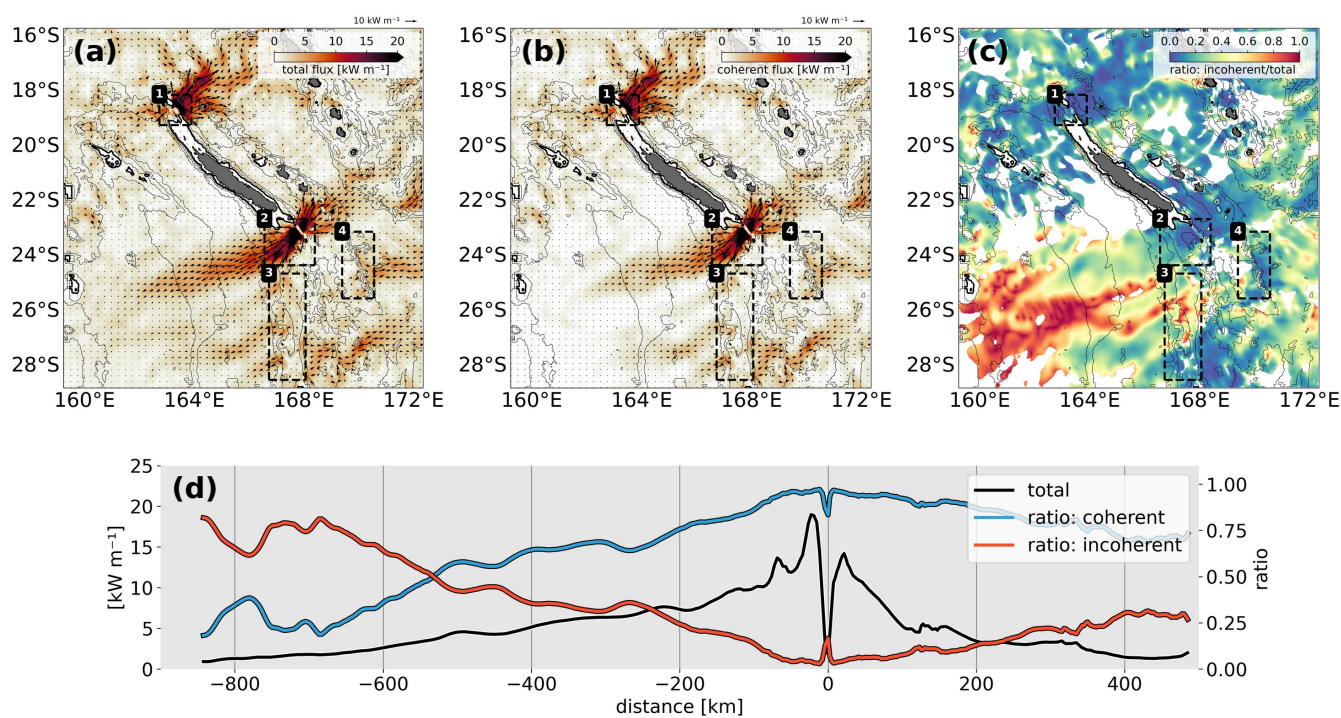
Figure 11. Annual mean of the (a) total and (b) coherent semidiurnal baroclinic energy flux including flux vectors. (c) The incoherent semidiurnal baroclinic energy flux is expressed as the ratio to the total semidiurnal internal tide. Regions with a total semidiurnal energy flux of < 1 kW m^{-1} are masked. Bathymetry contours and the black boxes are given as in Fig. 1b. (d) Total semidiurnal energy flux and the ratio of the coherent/incoherent tide to the total tide as a function of distance to the generation site (0 km, Pines Ridge), and averaged for the red box as indicated in (c).
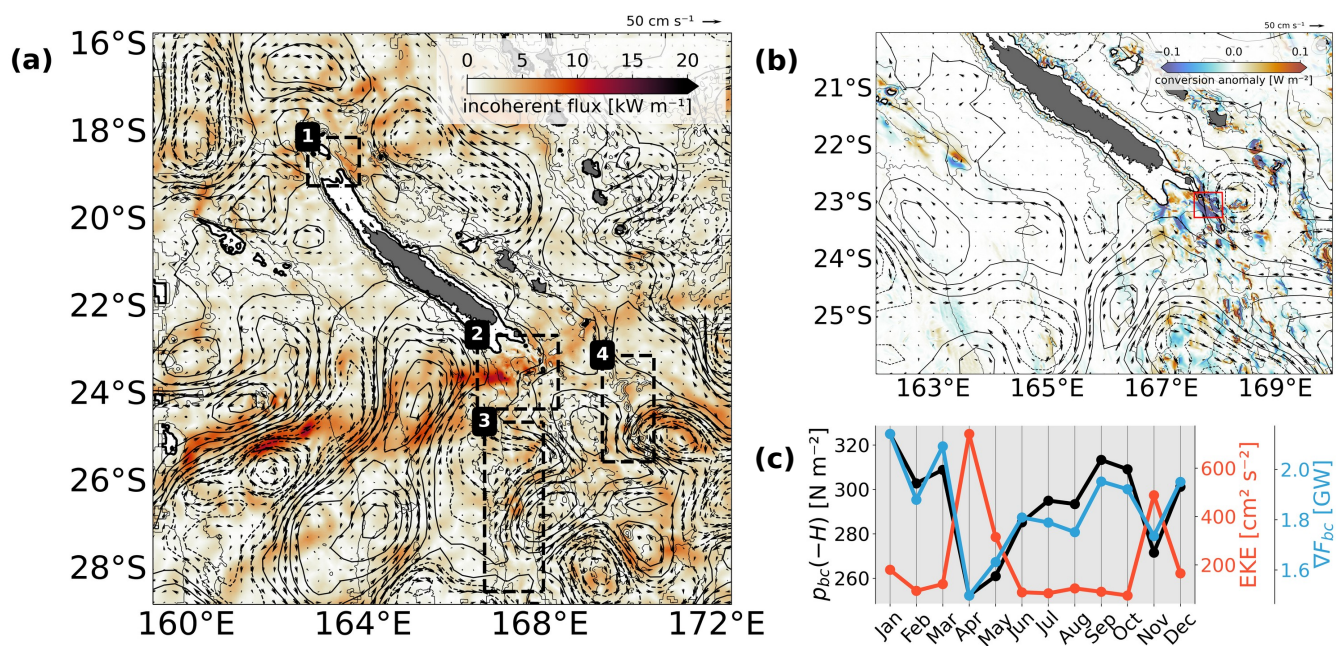
Figure 12. (a) Snapshot of the 5-day mean depth-integrated semidiurnal incoherent energy flux (shading) overlaid by the associated snapshot of the mesoscale eddy field from January 31 2014, i.e. geostrophic velocities vectors and sea level anomaly (SLA) contours (solid: SLA >0, dashed: SLA < 0). Bathymetry contours and the black boxes are given as in Fig. 1b. (b) M2 barotropic-to-baroclinic conversion anomaly (shading) for April 2014 relative to the coherent conversion term obtained from the annual tidal analysis overlaid by a representative snapshot of the 5-day mean mesoscale eddy field (see (a) for description) from 26 April 2014. (c) Monthly M2 baroclinic pressure amplitude at the ocean bottom $p_{bc}(-H)$ and the mesoscale EKE averaged for the Pines Ridge region (red box). Also shown is the monthly M2 depth-integrated baroclinic flux divergence ∇F_{bc} integrated over the Pines Ridge region.
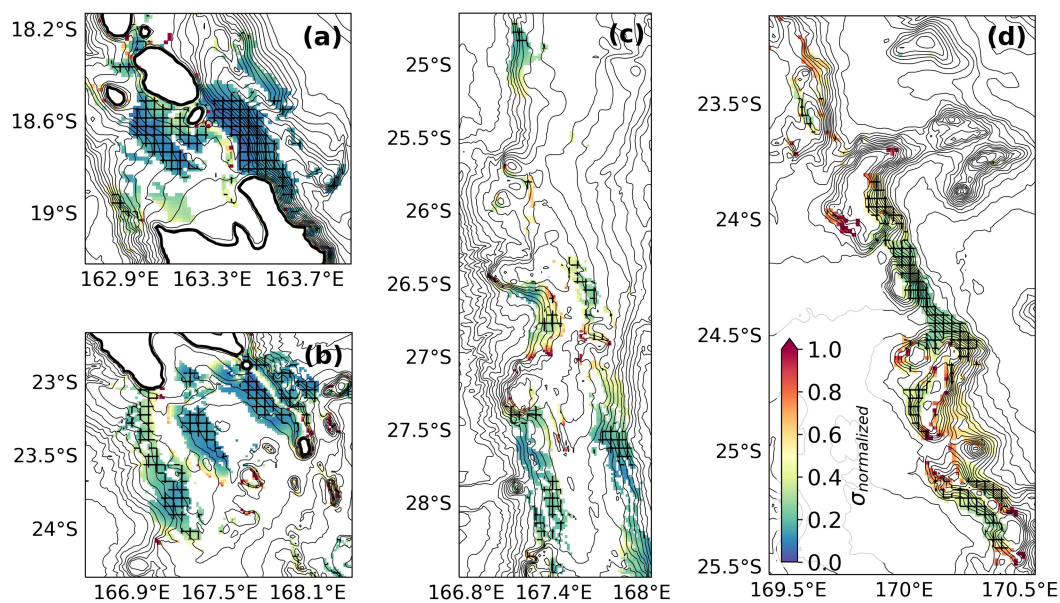
Figure 13. Standard deviation of the barotropic-to-baroclinic conversion term normalized by the annual mean conversion for (a) *North*, (b) *South*, (c) *Norfolk Ridge*, and (d) *Loyalty Ridge*. Grid points with conversion rates < 0.1 W m^{-2} are neglected from the analysis to account only for conversion that is associated with the generation hot spots. The hatched contours represent the regions where conversion variability is dominated by pressure amplitude variations. The depth contour interval is 200 m where the thick black line is the 100 m depth contour representative for the New Caledonian lagoon.
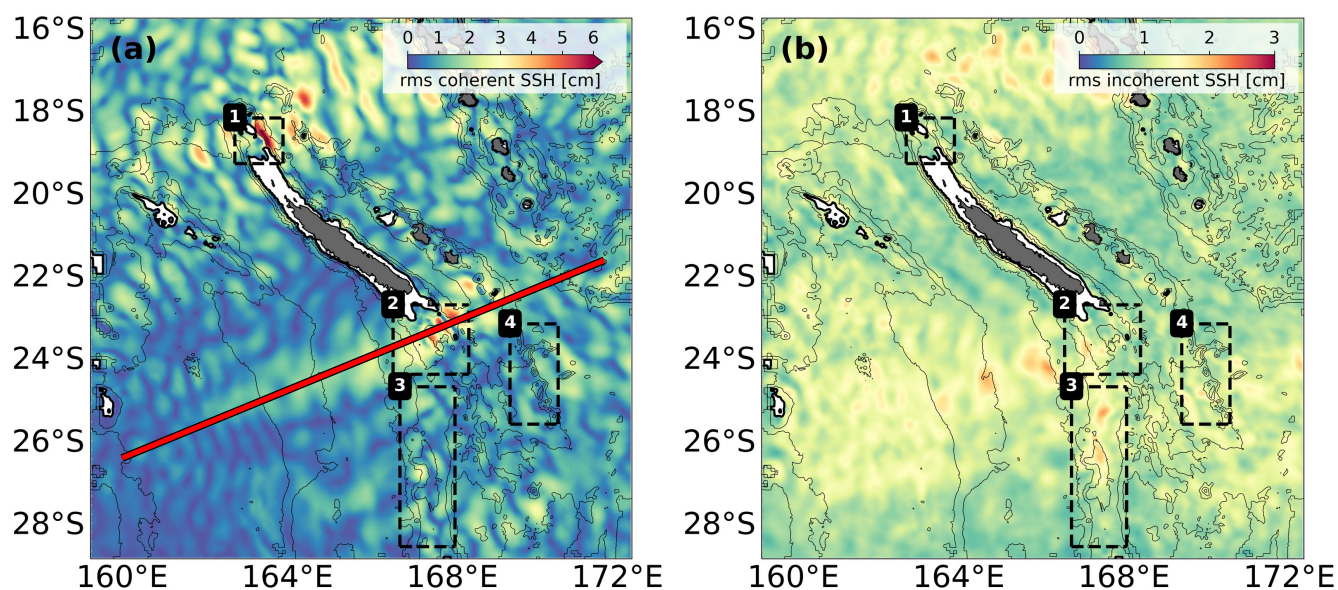
Figure 14. Annual root-mean-square (rms) of the (a) coherent and (b) incoherent semidiurnal SSH. Note the different colorbar scales. The red line indicates the transect in along-beam direction for which the SSH spectra are computed in Sect. 6.2. Bathymetry contours and the black boxes are given as in Fig. 1b.
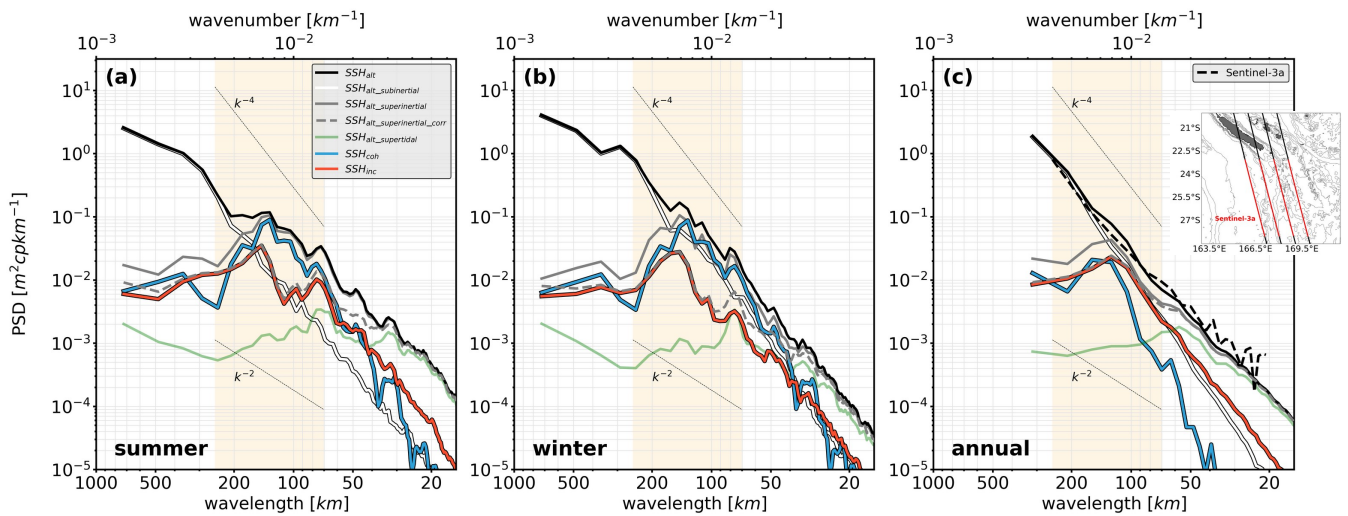
Figure 15. SSH wavenumber spectra in along-beam direction averaged for (a) summer (January-March) and (b) winter (July-September) months for the altimetry-like SSH (corrected for the barotropic tide, SSH_alt, black) with regard to the different dynamics that are separated in terms of frequency bands: subinertial (f < 1/36 h, SSH_alt_subinertial, white) for meso- and submesoscale dynamics, superinertial frequencies (f > 1/36 h, SSH_alt_superinertial, solid gray) for internal gravity waves by distinguishing between the coherent (SSH_coh, blue) and incoherent (SSH_inc, red) total (1/10 h - 1/28 h) internal tide. We also show the explicit contribution of supertidal frequencies (f > 1/10 h, SSH_alt_supertidal, green) to the superinertial frequency band. (c) SSH wavenumber spectra from a satellite altimeter point of view (Sentinel-3a, dashed black), for a ground track of 500 km length south of New Caledonia (inset) that resembles the nadir track of SWOT during its fast-sampling phase (cut at 20 km for visualization reasons). Note that model and altimetry spectra do not represent the same period (averaged for 2014 and 2016-2021, respectively). The altimetry-like SSH corrected for both the barotropic and baroclinic tide and filtered for motions at superinertial frequencies (SSH_alt_superinertial_corr, gray dashed) is also given. The characteristic wavenumber slopes k^{-2} and k^{-4} are represented by the dotted black lines. The mesoscale band (70-250 km) is highlighted by the yellow patch.

Table A1. Regional M2 barotropic energy flux divergence ∇F_{bt}, barotropic energy dissipation D_{bt}, barotropic-to-baroclinic conversion C, baroclinic energy flux divergence ∇F_{bc}, and baroclinic dissipation D_{bc} integrated over the *North*, *South*, *Norfolk Ridge*, *Loyalty Ridge* domains. The vertical structure for modes 1-4 are given for C and ∇F_{bc}.

		North	South	Norfolk Ridge	Loyalty Ridge
∇F_{bt}		-3.83	-6.16	-3.51	-1.28
D_{bt}		1.66	2.24	1.47	0.31
C	total	2.17	3.92	2.04	0.97
	mode-1	1.63	3.31	1.56	0.42
	mode-2	0.27	0.33	0.25	0.31
	mode-3	0.13	0.14	0.08	0.10
	mode-4	0.06	0.08	0.05	0.05
∇F_{bc}	total	1.47	1.83	0.96	0.53
	mode-1	1.30	1.58	0.86	0.38
	mode-2	0.16	0.20	0.09	0.12
	mode-3	< -0.01	0.02	< 0.01	0.01
	mode-4	0.01	0.01	< 0.01	0.01
D_{bc}	total	0.70	2.09	1.07	0.44

All units are given in [GW].